PARITOSH SINGH

DISSERTATION

Investigating the impact of Gold substrate on Molybdenum Disulfide

Supervisor

Prof. Dr. Claudia A. Draxl
Theoretische Festkörperphysik
Institut für Physik
Humboldt-Universität zu Berlin

Co-Supervisor

Dr. Ronaldo Rodrigues Pelá
Zuse Institute Berlin

UM-DAE

CENTRE FOR EXCELLENCE IN BASIC SCIENCES MUMBAI

Contents

Acknowledgement

I would like to express my gratitude to my supervisor, ***Prof. Dr. Claudia A. Draxl*** *and co-supervisor,* ***Dr. Ronaldo Rodrigues Pelá*** *for their constant support and guidance throughout my thesis project. This project has provided me with valuable insights into computational materials science. I have had the opportunity to learn new software tools and improve my theoretical and computational understanding in this field. I am also grateful to* ***Ignacio Gonzalez Oliva*** *and* ***Sven Lubeck****, PhD students, for assisting me with my analysis and report.*

I would also like to thanks ***Dr. Swapan K Ghosh****, Dean-Academics UM-DAE CEBS Mumbai. Without his support, this project would not have been successful. I would like to take this opportunity to thank the HOD of my institute* ***Dr. Sangita Bose*** *and the Project Coordinator,* ***Dr. Brijesh Prithvi*** *for their constant support throughout this project.*

I gratefully acknowledge the support from ***Humboldt-Universität zu Berlin*** *for their generous funding and infra structure to support my stay and the project. I am thankful to the computing time granted by the Resource Allocation Board and provided on the supercomputer* ***Lise*** *at* ***NHR@ZIB*** *as part of the NHR infrastructure.*

Last but not the least I am grateful to my parents and friend for their moral support throughout this project

Chapter 1

Introduction and Motivation

In modern materials science, two-dimensional (2D) materials have attracted considerable attention in theoretical, experimental, and computational research. With the isolation of graphene by Novoselov and Geim in 2004 [1], 2D materials have attracted enormous research interest due to their quantum effects and intriguing properties. These materials have paved the way for exploring fundamental chemistry and physics at the limit of single-atom thickness, and have the potential to unlock new technologies that were previously unattainable with other materials. In addition to application based research, these materials have also contributed in realizing several concepts in fundamental physics. For instance, the linear band dispersion of graphene near the K point [2]- has enabled researchers to explore the physics of mass-less Dirac Fermions. Moreover, the change in effective dimensionality leads to a larger specific surface area, presenting an appealing opportunity in the field of surface physics. The unique properties of 2D materials is studied for their diverse applications in catalysis, supercapacitors, energy storage devices, and high-performance sensors [3].

In the past decades a new class of 2D material, transition metal dichalcogenides (TMDCs), has gained significant attention. These atomically thin sheets, derived from layered materials, share many interesting characteristics with graphene, such as excellent electronic properties, exceptional mechanical flexibility, and partial optical transparency [4]. The general formula for TMDCs is of the MX_2 type, where M is a transition metal from the IVB and VIIB groups. These transition metals include Ti, V, Cr, Mn, Zr, Nb, Mo, Tc, Hf, Ta, W, and Re. X represents the chalcogenides, specifically S, Se, and Tl [5]. Unlike graphene, most of these materials are direct band gap semiconductors. Their properties can be tuned without any surface modifications [6]. Furthermore, these 2D nanosheets typically have a well-defined crystalline structure with few surface dangling bonds that traditionally plague most semiconductor nanostructures.

Among TMDCs, molybdenum disulfide (MoS_2) is a material that has garnered significant interest because of its low cost, earth abundance, chemical stability, wide negative potential range, and high specific capacitance [7]. MoS_2 in its bulk phase is made up of vertically stacked planes with covalently bonded S-Mo-S atoms closely packed in a hexagonal pattern. The adjacent hexagonal layers are held together via weak van der Waals interactions between neighboring S–S layers. MoS_2 is a semiconductor in both its bulk and 2D phases. The bulk phase has an indirect band gap of 1.2 eV [8], with a valence band maxima (VBM) at Γ point and the conduction band minima (CBm) at T point, which is halfway between Γ and K. This is illustrated in Fig. 1.1. While 2D MoS_2 exhibits a direct gap of 2.5 eV [9–11] at the K point. The transition from

indirect-to-direct band gap is correlated with changes in mechanical strength, spin density, bond energy, electrical conductivity, and the properties of transistor and sensor devices.

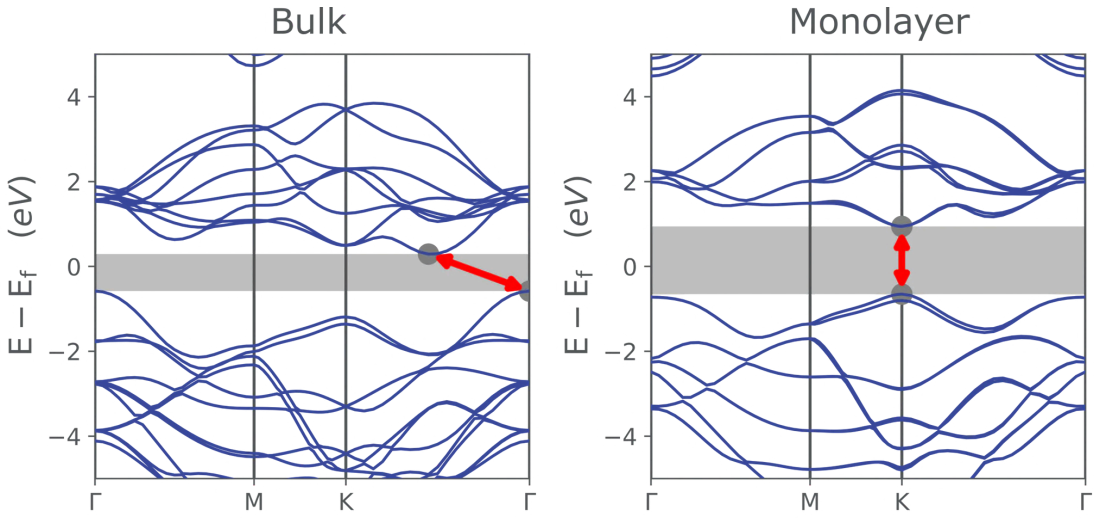

Fig. 1.1: Band structure diagram of bulk (left) and monolayer MoS2 (left) showing the crossover from indirect to direct band gap accompanied by a widening of the band gap [8].

One of the key factors for the wide use of MoS_2 is its tunable band gap, which changes with layer thickness, structure, and underlying substrate. The change in band gap of MoS_2 from one dimension to another, changes the photoluminescence characteristics of the material. Different band gaps mean tunable photoresponsivity, photoluminescence, absorption, and photoconductivity [12]. This allows for greater flexibility in using MoS_2 in a wide range of optoelectronic applications [13]. MoS_2 also exhibits high electron mobility [14, 15], and moderate spin-orbit coupling (SOC), which allows for exploiting its spin and valley degrees of freedom [16, 17]. The direct fundamental band gap makes it well-suited candidate to construct inter-band tunnel field-effect transistors (FETs). These transistors offer lower power consumption, high internal gain, and are capable of supporting high current densities [15].

The flexibility offered by monolayer TMDCs, however comes with a cost. These atomically thin layers are highly sensitive to the surrounding environment. They exhibit a strong Coulomb interaction associated with weak dielectric screening in two dimensions. As a consequence, the effect of polarization of the underlying substrate is significant. For instance, contacting MoS_2 with metal electrodes presents a significant challenge. Metallic substrates have the potential to modify electron-electron and electron-hole interactions, thereby re-normalizing electronic and quasi-particle properties [18]. The complexity further heightened if the monolayer-substrate interaction leads to formation of interface states [19]. The goal of this thesis is to investigate of gold (Au) substrate upon a 2D monolayer of MoS_2. We varied the thickness of substrate and analyzed its effect on band structure and density of state (DOS). In order to describe the Coulomb screening more accurately we further supplemented our calculation with state of the art G_0W_0 calculation.

Chapter 2

Theoretical aspects

2.1 Density Functional Theory

Density functional theory (DFT) is a powerful tool for analyzing the properties of molecules and materials. It provides reasonably good agreement with experimental results at a relatively lower computational cost compared to other ab initio methods. This offers a good compromise between accuracy and computational cost. In this method, the electron density is treated as the central variable instead of many-electron wavefunction. The inclusion of electron density results in a significant reduction in the computational cost by transforming the problem of $3N$ variables in electronic wavefunctions to only 3 variables in density. Its origin can be traced back to the 1920s. At that time, Thomas and Fermi developed a description of many-electron systems using the electron density $n(\mathbf{r})$ as the basic quantity, instead of the many-body wave function. The Thomas-Fermi method, as presented in 1927 [20], provided a framework for simplifying complex terms in the kinetic energy and electron-electron repulsion energy contributions to the total energy using relatively simple functionals of the electron density $n(\mathbf{r})$. However, it performed poorly when applied to real-world systems, producing inaccurate quantitative predictions and failing to reproduce some general features of density, such as shell structure in atoms and phenomena like bonding. The work by Hohenberg, Kohn, and L.J. Sham [21, 22] of the 1960's marked the starting point in the development of modern DFT.

The following section briefly summarizes the fundamentals of DFT. First, the fundamental lemma of the Hohenberg-Kohn [21] is presented, which serves as the foundation for the subsequent development of the Kohn-Sham (KS) equation [22]. The most important approximations of the KS formalism, the exchange-correlation (xc) potential, are then presented, along with their applications and limitations. Finally, the section concludes with a discussion of the implementation of DFT in the `exciting` code.

2.1.1 The Hohenberg–Kohn formulation

For a system of N interacting electrons, under Born–Oppenheimer approximation, the total energy can be expressed as a sum of terms involving only electrons and the effect of the external

potential $v_{ext}(\mathbf{r})$ due to nuclei and other external fields [23].

$$E = \langle \Psi | H | \Psi \rangle = \langle \Psi | T + V_{ee} | \Psi \rangle + \int d\mathbf{r} v_{ext}(\mathbf{r}) n(\mathbf{r}) \tag{2.1}$$

where E is the total energy of the system, $\Psi = \Psi(\mathbf{r_1}, \mathbf{r_2}, \ldots, \mathbf{r}_N)$ is a many body wavefunction, $\hat{T} = \sum_i -\frac{1}{2}\nabla_i^2$ is the total kinetic energy of electrons, V_{ee} is the Coulomb repulsion term, and $n(\mathbf{r})$ is the density. Hohenberg and Kohn in their seminal paper [21], proposed two theorems which formed the foundation of DFT. The two theorems are:

- The groundstate density $n_0(\mathbf{r})$ of a bound system of interacting electrons in some external potential $v_{ext}(\mathbf{r})$ determines this potential uniquely.
- The total energy of the system for any given $v_{ext}(\mathbf{r})$ can be written as a universal functional of the density $n(\mathbf{r})$. For any particular external potential, the exact ground state energy of the system is the global minimum value of this functional, and the density $n(\mathbf{r})$ that minimizes the functional is the exact ground state density $n_0(\mathbf{r})$.

An important consequence of these theorems for many-body systems is that the ground-state electron density $n_0(\mathbf{r})$ is adequate for determining the external potential that affects the system. Now, for systems with a fixed number of particles N, the only thing that varies from one system to another is the external potential $v_{ext}(\mathbf{r})$. Thus, $v_{ext}(\mathbf{r})$ uniquely determines the Hamiltonian of the system. Consequently, all properties derived from H are functional of the ground-state electron density $n_0(\mathbf{r})$.

Within the framework of DFT, the total energy of the system can be written as a functional of electron density [24]:

$$E_{v_{ext}(\mathbf{r})}[n(\mathbf{r})] = \int v_{ext}(\mathbf{r}) n(\mathbf{r}) d\mathbf{r} + F[n(\mathbf{r})] \tag{2.2}$$

where, $F[n(\mathbf{r})] = \langle \Psi[n(\mathbf{r})] | T + V | \Psi[n(\mathbf{r})] \rangle$ being the universal functional of density. From here, it is possible to obtain the ground state energy by variational minimization of E with respect to the electronic density $n(\mathbf{r})$. This idea was first introduced by Hohenberg and Kohn, but later Levy [25] and Lieb [26] gave a more succinct derivation, known as the *constrained search method*.

The basic idea of this method is to divide the minimization procedure into two steps. Firstly, the trial density $n(\mathbf{r})$ is fixed and the minimization is performed within the set of trial wave functions, denoted by $\Psi_n^\alpha(\mathbf{r})$, corresponding to $n(\mathbf{r})$ [27]. The constrained energy minimum with $n(\mathbf{r})$ is given by

$$\begin{aligned} E &= min_\alpha \langle \Psi_n^\alpha(\mathbf{r}) | H | \Psi_n^\alpha(\mathbf{r}) \rangle \\ &= \int v_{ext}(\mathbf{r}) n(\mathbf{r}) + F[n(\mathbf{r})] \end{aligned}$$

where, $F[n(\mathbf{r})] = min_\alpha \langle \Psi_n^\alpha(\mathbf{r}) | T + V | \Psi_n^\alpha(\mathbf{r}) \rangle$. As a result of this minimization, one obtains the wavefunction for a fixed density with respect to which the energy is minimum. In the next step, the minimization with respect to density is carried out.

$$E = min_{n(\mathbf{r})} E_{v(r)}[n\mathbf{r}]$$

$$E = min_{n(\mathbf{r})} \int v_{ext}(\mathbf{r}) n(\mathbf{r}) + F[n(\mathbf{r})] \tag{2.3}$$

For a non-degenerate groundstate, the minimum is attained when $n(r)$ is the ground-state density and, for the case of a degenerate ground state, $n(r)$ is any one of the ground-state densities among all degenerate states. Thus, the formidable problem of finding the energy minimum for a $3N$ dimensional system of wavefunction $\Psi(\mathbf{r}_1, \mathbf{r}_2, \ldots, \mathbf{r}_N)$ with $\mathbf{r} = (\mathbf{x}, \mathbf{y}, \mathbf{z})$, reduces to just a 3-dimensional system involving density $n(\mathbf{r})$ using the HK formalism.

2.1.2 Kohn-Sham equations

Hohenberg Kohn formalism partially remedies the problem by reducing it from $3N$ dimensions to just 3 dimension. However the exact description of the solution depends upon the definition of $F[n(\mathbf{r})]$. Hohenberg and Kohn suggested to rewrite this functional as [21, 27]

$$F[n(\mathbf{r}) = T_s[n(\mathbf{r})] + \frac{1}{2} \iint d\mathbf{r} d\mathbf{r}' \frac{n(\mathbf{r}) n(\mathbf{r}')}{|\mathbf{r} - \mathbf{r}'|} + E_{xc}[n(\mathbf{r})]] \tag{2.4}$$

where $T_s[n(\mathbf{r})]$ represents the kinetic energy functional for non-interacting electrons, the second term represents the Coulomb interaction energy. The last term, $E_{xc}[n(\mathbf{r})]$, is the so-called exchange-correlation energy, which takes into account all the many-body effects which is not captured in the independent particle picture. Using this definition, Eq. (2.3) can be re-written as [27]:

$$E_{v_{ext}(\mathbf{r})}[n(\mathbf{r})] = \int v_{ext}(\mathbf{r}) n(\mathbf{r}) d\mathbf{r} + T_s[n(\mathbf{r})] + \frac{1}{2} \iint d\mathbf{r} d\mathbf{r}' \frac{n(\mathbf{r}) n(\mathbf{r}')}{|\mathbf{r} - \mathbf{r}'|} + E_{xc}[n(\mathbf{r})] \tag{2.5}$$

Evaluation of Eq. (2.5) for some arbitrary electron density gives energy $E_{v_{ext}(\mathbf{r})} > E_0$, where E_0 is the ground-state energy. Therefore, one needs to minimize Eq. (2.5) with respect to density under the constraint

$$\int n(\mathbf{r}) d\mathbf{r} = N$$

The corresponding Euler-Lagrange equations, for a given total number of electrons has the form:

$$\int \delta n(\mathbf{r}) \big\{ v_{ext}(\mathbf{r}) + \int \frac{n(\mathbf{r})}{|\mathbf{r} - \mathbf{r}'|} d\mathbf{r}' + \frac{\delta T_s[n(\mathbf{r})]}{\delta n(\mathbf{r})} + \frac{\delta E_{xc}[n(\mathbf{r})]}{\delta n(\mathbf{r})} - \epsilon \big\} d\mathbf{r} = 0, \tag{2.6}$$

where ϵ is the Lagrange multiplier. Now, one can separate the kinetic energy part from the rest of the equation and can re-write it as

$$\int \delta n(\mathbf{r}) \big\{ \frac{\delta T_s[n(\mathbf{r})]}{\delta n(\mathbf{r})} + v_{eff}(\mathbf{r}) - \epsilon \big\} d\mathbf{r} = 0 \tag{2.7}$$

This expression now looks very similar to a system of non-interacting particles (with wavefunction $\psi_i(\mathbf{r})$) moving in an external field of effective potential $v_{eff}(\mathbf{r})$, which corresponds to a Schrodinger like equation

$$\left[-\frac{1}{2} \nabla^2 + v_{eff}(\mathbf{r}) \right] \psi_i(\mathbf{r}) = \epsilon_i \psi_i(\mathbf{r}) \tag{2.8}$$

which has to be solved self consistently. Starting with the initial guess one self-consistently solves Eq. (2.7) to get minimum density and potential with

$$n(\mathbf{r}) = \sum_{j=1}^{N} |\psi_j(r)|^2 \tag{2.9}$$

$$v_{eff}(\mathbf{r}) = v(\mathbf{r}) + \int \frac{n(\mathbf{r}')}{|\mathbf{r} - \mathbf{r}'|} d\mathbf{r}' + v_{xc}(\mathbf{r}) \tag{2.10}$$

where v_{xc} is the *local* exchange-correlation potential defined as $\frac{\delta E_{xc}}{\delta \tilde{n}(r)}\big|_{\tilde{n}(r)=n(r)}$. Eq. (2.7), (2.9), and (2.10) forms the self consistent Kohn-Sham equations with $\psi_i(\mathbf{r})'s$ and $\epsilon_i' s$ are the KS wavefunctions/orbitals and eigenvalues respectively.

The KS theory can be regarded as an exact theory if we can obtain the correct expression for v_{xc} and E_{xc}. Thus the practical usefulness of DFT depends entirely upon the approximation for exchange-correlation terms. The next section briefly discusses about most widely used *Local Density Approximation (LDA)* and *Generalized Gradient Approximation (GGA)* levels of approximations for exchange-correlation potential. There are few remarks to end this section.

1. The exact effective single-particle potential $v_{eff}(\mathbf{r})$ of KS theory, Eq. (2.7) can be regarded as that unique, fictitious external potential which leads, for noninteracting particles, to the same physical density $n(\mathbf{r})$ as that of the interacting electrons in the physical external potential $v_{ext}(\mathbf{r})$. Thus if the physical density $n(\mathbf{r})$ is independently known (from experiment or for small systems—from accurate, wavefunction-based calculations) $v_{eff}(\mathbf{r})$ and hence also $v_{xc}(\mathbf{r})$ can be directly obtained from the density $n(\mathbf{r})$

2. Neither the exact KS wavefunction ($\psi_j' s$), nor the eigenvalues ($\epsilon_j' s$) have any direct physical significance except for the fact that KS orbitals are linked with the density of the physical system by Eq. (2.9) and the eigenvalue of highest occupied state (ϵ^{HOMO}), equals the ionization energy [28].

2.1.3 Exchange-Correlation functionals

So far, our discussion has presented a formal framework for understanding many-body problem from the perspective of the electron density, $n(r)$. However, to utilize it, we need accurate approximations for $E_{xc}[n(r)]$. The success of KS-DFT is attributed to the fact that even simple approximate functionals can yield remarkably accurate results for the ground state properties of many systems. The most important approximation for $E_{xc}[n(r)]$ is the quasi-local form [27]. The expression for $E_{xc}[n(r)]$ can be written as [27]:

$$E_{xc}[n(r)] = \int e_{xc}(r; [n(\tilde{r})]) n(r) dr \tag{2.11}$$

where $e_{xc}(r; [n(\tilde{r})])$ represents the exchange-correlation energy per particle at the point r, and it is the functional of density distribution $n(\tilde{r})$ near point r. The definition of "near" is of the order of the local Fermi wavelength. The simplest of approximation for $E_{xc}[n(r)]$ is the so called **Local Density Approximation (LDA)**,

$$E_{xc}^{LDA} \equiv \int e_{xc}(n(r)) n(r) dr$$

where $e_{xc} = e_x + e_c$ is the exchange-correlation energy per particle of a uniform electron gas of density n [22]. The exchange part is given, in atomic units, by:

$$e_x = -\frac{0.458}{r_s} \tag{2.12}$$

where r_s is defined from the equation $(4\pi/3)r_s^3 = n^{-1}$. The correlation energy density has been calculated numerically for a set of densities using quantum Monte Carlo[29, 30] and interpolated in various forms. It was first estimated by E.P. Wigner [31]:

$$\epsilon_c = -\frac{0.44}{r_s + 7.8} \tag{2.13}$$

Although originally expected to be valid only for slowly varying densities, the LDA has also been successful for inhomogeneous systems. When it comes to accuracy, the exchange energy typically differs by approximately 10%, while the correlation energy tends to be overestimated by up to twice its actual value [32]. However, these errors often balance each other out to some extent. LDA provides reasonably accurate results (around 10-20% error) for ionization energies, dissociation energies, and cohesive energies of atoms and molecules [33]. Surprisingly, it performs well in predicting bond lengths and geometries with an overall accuracy of around 1% [27, 33].

The LDA is the "mother" of almost all approximations currently in use in DFT. To improve its accuracy, one possibility is to include the gradient of the electron density in the description of $E_{xc}[n(r)]$. The xc functional in the GGA takes the form [24, 27]

$$E_{xc}^{GGA}[n(\mathbf{r})] = \int \epsilon_{xc}(n(\mathbf{r}), |\nabla n(\mathbf{r})|) n(\mathbf{r}) d\mathbf{r} \tag{2.14}$$

Substituting the LDA with GGA's has resulted in a reduction of errors in atomization energies for typical sets of small molecules composed of light atoms by factors ranging from 3 to 5 [34].

2.1.4 Implementation in `exciting`

`exciting` [35] is a full-potential all-electron density-functional-theory package implementing Linearized Augmented Planewave methods and local orbitals ([L]APW[+LOs]) as basis functions. The APW related methods are highly precise all-electron schemes for describing solids. Due to their high precision, the methods employing these basis sets are considered as the gold standard of DFT for extended systems [36].

(L)APW(+LO's)

One particular problem that arises while solving KS equation is how to efficiently represent KS wavefunctions for electrons without sacrificing accuracy. These wavefunctions exhibit smooth and gradual variations in the regions between atoms. However, in the vicinity of nuclei, they show significant variations. This behavior is common to both core and valence states. The wavefunctions of the former are strongly localized around nuclei, while those of the latter rapidly oscillate to satisfy the orthogonality condition. Methods based on linear combinations of atomic orbitals or pseudopotentials provide solutions to this problem, but they either lack high numerical accuracy or are oversimplified for certain problems. Thus, despite their usefulness, they cannot be regarded as the ultimate reference in condensed matter applications.

The (Linearised) Augmented Plane wave method is considered to be a state-of-the-art technique capable of accurately describing the system. In this method, the space is partitioned into two regions: muffin-tin (MT) regions, which are a set of non-overlapping spheres centered around each atom in the system, and interstitial ($\mathbb{I}$). Please refer to figure 2.1 for a visual representation of the partitioning, where the wavefunctions are described differently. The space inside the muffin tin region is expanded in terms of a linear combination of radial solutions of the KS equation, while interstitial regions are represented by plane waves [35–37].

$$\Phi_{\mathbf{G}+\mathbf{k}}(\mathbf{r}) = \begin{cases} \sum_{lm}[A^{\mathbf{G}+\mathbf{k}}_{lm\alpha} u_{l\alpha}(r_\alpha) + B^{\mathbf{G}+\mathbf{k}}_{lm\alpha} \dot{u}_{l\alpha}(r_\alpha)]Y_{lm}(\hat{\mathbf{r}}_\alpha), & r_\alpha \leq R_{MT} \\ \frac{1}{\sqrt{\Omega}} \exp \iota(\mathbf{G}+\mathbf{k})r, & r \in I \end{cases} \tag{2.15}$$

Here, $\mathbf{G}$ is the reciprocal lattice vector, and $\mathbf{k}$ is an arbitrary vector in reciprocal space lying in the First Brillouin Zone. Additionally, $\hat{Y}_{lm}(\hat{\mathbf{r}}_\alpha)$ represents the spherical harmonics. The $u^\alpha_l(r_\alpha)$ represents the radial solutions of the Schrödinger equation [35, 37] given by:

$$\Big\{ -\frac{1}{2}\frac{d^2}{dr^2} + \frac{l(l+1)}{2r^2} + v_0(r) - \epsilon_{\mathbf{l}} \Big\}(r u_{l\alpha}(r)) = 0 \tag{2.16}$$

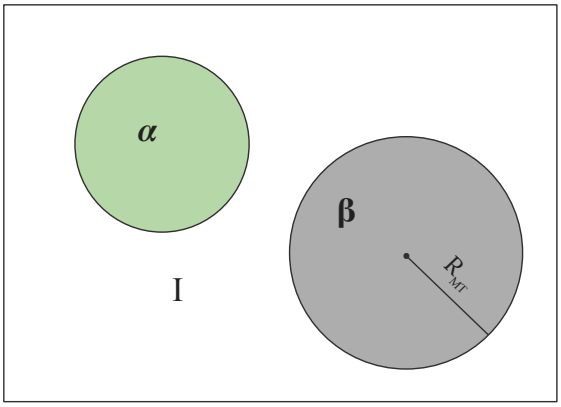

Fig. 2.1: Partitioning of space in LAPW method

here ϵ_l is the eigenvalue of the Eq. (2.8) for a given l, and v_0 represents the spherical component of the potential inside the atomic sphere α. $\dot{u}_{l\alpha}$ is the energy derivative of radial function $u_{l\alpha}$. Each plane wave is then augmented at the Muffin Tin boundary determined by its radius R_{MT}. The representation in the two regions is intuitive. Wavefunctions in the vicinity of nuclei are more accurately described using atom-centered functions combined with spherical harmonics, while plane waves efficiently describe smooth wavefunctions in the interstitial region. The coefficients A and B are chosen to ensure that the basis functions are continuous and differentiable at the boundaries of the sphere [35, 37].

Local Orbitals

By construction, the (Linearized) APW basis set leads to an accurate description of the energy bands, provided that the parameter ϵ_l is chosen close to the band energy of interest. This linearization, however, introduces the problem that only the states of one principal quantum number can be described for a given l value. This can indeed be a significant limitation in the treatment of low-lying valence states (semicore states). The semi-core states are neither tightly bound to the nucleus nor freely moving like valence electrons. Therefore, the appropriate way to treat them is to separately expand them for both energy windows. However, this method may encounter the issue of orthogonality between the eigenfunctions of the two windows. One solution to this problem is the extension of the LAPW method, in which more than two radial functions are matched to their counterparts in the interstitial [36, 38]. However, matching higher order derivatives causes this method to converge much more slowly with respect to the number

of basis functions.

A simpler approach to addressing this issue involves the use of so-called local orbitals (LOs) originally proposed by Singh [39]. These are additional basis functions introduced within the atomic spheres, with a form similar to that of the atomic-like functions in the LAPW basis set. The description of local orbitals as presented in [36] is

$$\phi_{LO} = [A^{\alpha}_{lm} u^{\alpha}_{l}(r, E_l) + B^{\alpha}_{lm} \dot{u}^{\alpha}_{l}(r, E_l)] \tag{2.17}$$

where A^{α}_{lm} and B^{α}_{lm} are determined so that the LO and its slope approach zero at the sphere boundary, ensuring that the basis function is entirely confined within the atomic sphere. These orbitals are not augmented by any plane waves; one must choose such functions for only some physically relevant states. It is important to note that this strategy of including LOs for physically relevant states is not limited to semi-core states. It can also be used to improve the description of conduction bands [36, 39].

`exciting` workflow

The KS equations is a non-linear problem and have to be solved self-consistently. Once the radial solution $u_{l\alpha}$ of Eq. (2.16) is determined, it is used to solve for the coefficients A and B in Eq. (2.15), which completely defines the basis set. Once the basis set is defined, it is used to solve for the Hamiltonian($H^{\mathbf{k}}$) and the over-lap matrices ($S^{\mathbf{k}}$). The matrix elements are given by [35]

$$H^{\mathbf{k}}_{\mathbf{G}\mathbf{G}'} = \langle \phi_{\mathbf{G}+\mathbf{k}} | -\frac{1}{2}\nabla^2 + v_{KS} | \phi_{\mathbf{G}'+\mathbf{k}} \rangle \tag{2.18}$$

and

$$S^{\mathbf{k}}_{\mathbf{G}\mathbf{G}'} = \langle \phi_{\mathbf{k}+\mathbf{G}} | \phi_{\mathbf{k}+\mathbf{G}'} \rangle \tag{2.19}$$

respectively. With the definition of matrices above, one can rewrite the KS equations as a matrix problem

$$H^{\mathbf{k}} C^{\mathbf{k}} = \epsilon^{\mathbf{k}} S^{\mathbf{k}} C^{\mathbf{k}}. \tag{2.20}$$

Here $C^{\mathbf{k}}$ is the coefficient vector of the wavefunction

$$\Psi_{i\mathbf{k}} = \sum_{\mathbf{G}} C^{\mathbf{k}}_{i\mathbf{G}} \phi_{\mathbf{G}+\mathbf{k}}(\mathbf{r}) + \sum_{\mu} C^{\mathbf{k}}_{i\mu} \phi_{\mu}(\mathbf{r}),$$

and the coefficients $C^{\mathbf{k}}_{i\mu}$ must satisfy two conditions: $\phi_{\mu}(\mathbf{r}) = 0$ at the MT boundary and $\int_{\Omega} |\phi_{\mu}(\mathbf{r})|^2 d\mathbf{r} = 1$. The function ϕ_{μ} is referred to as the local orbital. To make the problem numerically tractable, the dimension of the matrices $H^{\mathbf{k}}$ and $S^{\mathbf{k}}$ is made finite through the condition $|\mathbf{G} + \mathbf{k}| < \mathbf{G_{max}}$, where $\mathbf{G_{max}}$ is a planewave cutoff.

The process begins by initializing the Kohn-Sham potential, which is determined either by combining atomic densities or carried over from a previous DFT calculation. Subsequent stages involve exciting core wavefunctions and basis functions, creating Hamiltonian and overlap matrices, solving Eq. (2.20) for KS eigenenergies and wavefunctions, and adjusting the density and potential. This process continues until consecutive solutions closely align to meet the specified convergence criteria, as shown in Figure 2.2.

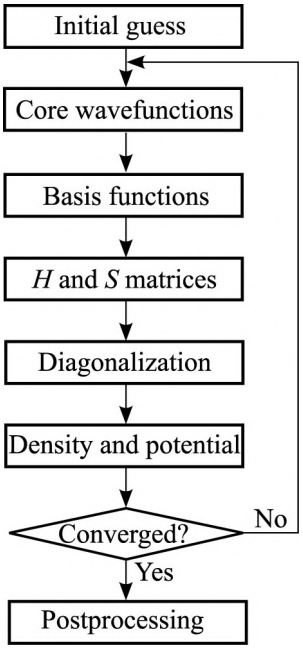

Fig. 2.2: Workflow for the self-consistent solution of the KS equation in the (L)APW+lo basis, taken from [35]

2.2 $G_0 W_0$

Kohn-Sham eigenvalues provide a reasonable zeroth-order approximation for the single-particle excitation energies. However, LDA fails to accurately describe the fundamental band gaps [40]. Kohn-Sham density functional theory (KS-DFT) has been successful in describing various properties of atoms, molecules, and solids. It allows for accurate treatment of very large systems at a reasonable computational cost. However, for systems involving correlation or screening, DFT fails to provide a reliable prediction of the properties of such materials. In practical applications of the original theory, these factors may all be considered to arise from the need to approximate the exchange-correlation functional. Conversely, the many-body Green function theory provides the theoretical framework for analyzing the experimentally observed quasiparticle band structure. This chapter provides a brief introduction to the Green function approach in the context of many-body electronic systems, with a specific focus on the $G_0 W_0$ approximation. The ideas are mainly derived from [41] and from Hedin and Lundqvist's seminal paper [42]. This section will establish the theoretical framework that will guide our numerical implementation and subsequent analysis of the outcomes discussed in this thesis.

2.2.1 Green's Function Formalism

The one-particle Green's function in time-ordered representation is given by:

$$G(\mathbf{r}, t; \mathbf{r}', t') = -\iota \langle N|\hat{T}\{\hat{\psi}(\mathbf{r}, t)\hat{\psi}^\dagger(\mathbf{r}', t')\}|N\rangle \tag{2.21}$$

where $\hat{\psi}(\mathbf{r}, t)$ and $\hat{\psi}^\dagger(\mathbf{r}', t')$ are the field operators that respectively annihilate and create the particles at their respective spacetime coordinates. The operator $\hat{T}$ is the time-ordering operator, which rearranges the field operators from right to left in ascending order of time to ensure

consistency with causality. The term inside the brackets represents the commutator of fermionic systems. The expectation value of the commutator is calculated with respect to the ground state $|N\rangle$ of the many-body Hamiltonian ($\hat{H}$).

In the Heisenberg representation, the field operator is expressed as:

$$\hat{\psi}(\mathbf{r},t) = e^{\iota\hat{H}t}\hat{\psi}(\mathbf{r})e^{-\iota\hat{H}t} \tag{2.22}$$

where $\hat{\psi}(\mathbf{r})$ is a field operator in the Schrödinger picture. Substituting Eq. (2.22) into Eq. (2.21) and using the notion of identity in the Fock space, i.e.

$$1 = \sum_N \sum_n |N,n\rangle \langle N,n|,$$

where N and n represent the number of particles and the excited state index of the system, the expression for the independent particle Green's Function becomes

$$\begin{aligned} G(\mathbf{r},t;\mathbf{r}',t') = &-\iota \sum_n \langle N|\hat{\psi}(\mathbf{r})|N+1,n\rangle\, e^{-\iota(E^s_{N+1}-E_N)(t-t')}.\, \langle N+1,n|\hat{\psi}^\dagger(\mathbf{r})|N\rangle\, \Theta(t-t') \\ &+\iota \sum_n \langle N|\psi^\dagger(\mathbf{r}')|N-1,n\rangle\, .e^{-\iota(E^n_{N-1}-E_N)(t-t')}\, \langle N-1,n|\hat{\psi(\mathbf{r})}|N\rangle\, \Theta(t'-t) \end{aligned}$$

Here, E_N represents the ground state energy of the N-electron system, and $E^n_{N\pm1}$ represents the n^{th} excited state of $N\pm1$ electron system, respectively. The time-ordered operator has been replaced with the Heaviside function. This expression can be further simplified by introducing the excitation energy ϵ_n and the amplitude ψ_s, which are defined as follows:

$$\begin{aligned} \epsilon_n = E^n_{N+1} - E_N,\ \psi_n(\mathbf{r}) = \langle N|\hat{\psi}(\mathbf{r})|N+1,n\rangle,\ \text{for } \epsilon_s \geq \mu \\ \epsilon_s = E_N - E^s_{N-1},\ \psi_n(\mathbf{r}) = \langle N-1,n|\hat{\psi}(\mathbf{r})|N\rangle,\ \text{for } \epsilon_s < \mu \end{aligned}$$

where μ is the chemical potential of the N-electron system ($\mu = E_{N+1} - E_N$). Thus, the simplified expression now looks like this:

$$\begin{aligned} G(\mathbf{r},\mathbf{r}';t-t') = -\iota \sum_n \psi_n(\mathbf{r})\psi^*_n(\mathbf{r}')e^{-\iota\epsilon_n(t-t')} \\ [\Theta(t-t')\Theta(\epsilon_s-\mu) - \Theta(t'-t)\Theta(\mu-\epsilon)] \end{aligned}$$

Performing a Fourier transform on this equation to the frequency axis, we obtain:

$$G(\mathbf{r},\mathbf{r}',\omega) = \lim_{\eta\to0} \sum_n \psi_n(\mathbf{r})\psi^*_n(\mathbf{r}')\Big[\frac{\Theta(\epsilon_n-\mu)}{\omega-(\epsilon_n-\iota\eta)} + \frac{\Theta(\mu-\epsilon_n)}{\omega-(\epsilon_n+\iota\eta)}\Big] \tag{2.23}$$

This representation is called the *Lehmann representation*. The key feature of Eq. (2.23) is that the Green function has singular poles that correspond to the exact excitation energies of the many-body system. For excitation energies larger (smaller) than the chemical potential, these singularities are located slightly below (above) the real axis in the complex frequency plane. The need of this formalism will become clear when we will discuss the interacting Hamiltonian of N particle system and arrive to Dyson Equation.

2.2.2 Dyson Equation

The Hamiltonian of an interacting system of N particles in second quantization is given by:

$$\hat{H} = \int d\mathbf{r}dt\hat{\psi}^{\dagger}(\mathbf{r},t)\Big[-\frac{\nabla^2}{2} + V_{ext}\Big]\hat{\psi}(\mathbf{r},t) + \frac{1}{2}\iint d\mathbf{r}dtd\mathbf{r}'dt'\hat{\psi}^{\dagger}(\mathbf{r},t)\hat{\psi}(\mathbf{r}',t')\frac{1}{|\mathbf{r}-\mathbf{r}'|}\hat{\psi}(\mathbf{r}',t')\hat{\psi}(\mathbf{r},t)$$

where ψ and $\psi^{\dagger}$ are field operators. The time evolution of these field operators in the Heisenberg representation is governed by the equation of motion:

$$\iota\frac{\partial}{\partial t}\hat{\psi}(\mathbf{r}.t) = [\hat{\psi}(\mathbf{r},t), \hat{H}] \tag{2.24}$$

By evaluating this commutator using the above expression for the Hamiltonian, one can obtain the equation of motion for the single-particle Green's function:

$$\Big[\iota\frac{\partial}{\partial t} + \frac{1}{2}\nabla^2 - V_{ext}(\mathbf{r})\Big]G(\mathbf{r},t;\mathbf{r}',t') + \iota\int d\mathbf{r}_1\frac{1}{|\mathbf{r}-\mathbf{r}_1|}\langle N|\hat{T}[\hat{\psi}^{\dagger}(\mathbf{r}_1,t)\hat{\psi}(\mathbf{r}_1,t)\hat{\psi}(\mathbf{r},t)\hat{\psi}^{\dagger}(\mathbf{r}',t')]|N\rangle = \delta(\mathbf{r}-\mathbf{r}')\delta(t-t') \tag{2.25}$$

The quantity in the middle of the equation represents the two-particle Green function. Following similar procedure for two-particle GF, one ends up with the term for the three-particle GF. This way, the hierarchy continues. To simplify this representation, we define a mass operator M as:

$$\int d\mathbf{r}_1dt_1M(\mathbf{r},t;\mathbf{r}_1,t_1)G(\mathbf{r}_1,t_1;\mathbf{r}',t') = -\iota\int d\mathbf{r}_1v(rb-\mathbf{r}_1)\langle N|\hat{T}[\hat{\psi}^{\dagger}(\mathbf{r}_1,t)\hat{\psi}^{\dagger}\hat{\psi}(\mathbf{r},t)\hat{\psi}(\mathbf{r}',t')]|N\rangle$$

Using this definition of the mass operator, the expression in Eq. (2.25) can be rewritten as:

$$\Big[\iota\frac{\partial}{\partial t} + \frac{1}{2}\nabla^2 - V_{ext}(\mathbf{r})\Big]G(\mathbf{r},t;\mathbf{r}',t') - \int d\mathbf{r}_1dt_1M(\mathbf{r},t;\mathbf{r}_1,t_1)G(\mathbf{r}_1,t_1;\mathbf{r}',t') = \delta(\mathbf{r}-\mathbf{r}')\delta(t-t') \tag{2.26}$$

Since the Hartree interaction is a one-particle operator, it is typically separated from the mass operator M to define the self-energy as $\Sigma = M - V_H$. By substituting the Σ in Eq.(2.26) we finally arrive at the following expression:

$$\Big[\iota\frac{\partial}{\partial t} - H_0\Big]G(\mathbf{r},t;\mathbf{r}',t') - \int d\mathbf{r}_1dt_1\Sigma(\mathbf{r},t;\mathbf{r}_1,t_1)G(\mathbf{r},t;\mathbf{r}',t') = \delta(t-t')\delta(r-r') \tag{2.27}$$

where,

$$H_0 = -\frac{1}{2}\nabla^2 + V_{ext}(\mathbf{r}) + V_H(\mathbf{r})$$

Now, multiplying Eq. (2.27) by G_0 from the left, we deduce the well-known Dyson equation.

$$G(\mathbf{r},t;\mathbf{r}',t') = G_0(\mathbf{r},t;\mathbf{r}',t')+ \iint d\mathbf{r}_1 d\mathbf{r}_2 dt_1 dt_2 G_0(\mathbf{r},t;\mathbf{r}_2,t_2)\Sigma(\mathbf{r}_2,t_2;\mathbf{r}_1,t_1)G(\mathbf{r}_1,t_1;\mathbf{r}',t') \quad (2.28)$$

Here, we have used the fact that under Hartree approximation, Eq. (2.27) reduces to:

$$\Big[\iota\frac{\partial}{\partial t} - H_0\Big]G_0(\mathbf{r},t;\mathbf{r}',t') = \delta(t-t')\delta(r-r'). \quad (2.29)$$

We can continue in this manner by recursively replacing G on the right-hand side, which leads to a series expansion.

$$G = G_0 + G_0\Sigma G_0 + G_0\Sigma G_0\Sigma G_0 + \dots \quad (2.30)$$

This series is known as the **Dyson Series** which demonstrates that the single-particle propagator $G(\mathbf{r},t;\mathbf{r}',t')-$ is equal to the "free" particle propagator $G_0(\mathbf{r},t;\mathbf{r}',t')$ plus the sum of the probability amplitudes of propagating from $(\mathbf{r},t)$ to $(\mathbf{r}',t')$ after single, double, etc., scattering processes, with Σ playing the role of the scattering potential.

2.2.3 G_0W_0 Approximation

The actual derivation of the G_0W_0 equation would be quite tedious and is also not necessary for the work of this thesis. Interested readers can refer to the following sources [42, 43] for detailed derivations. This section discusses the state-of-the-art G_0W_0 approach. The G_0W_0 method functions as a correction for KS eigenvalues. Starting with the theoretical aspects of G_0W_0, the section subsequently discusses its implementation in the exciting code, examining how it was executed.

Although the Density Functional Theory (DFT) may not be highly accurate, it serves as a significantly better tool for qualitative understanding of any real system. It enables us to comprehend that while the V^{xc} functional of DFT is capable of capturing the many-body interactions within the exchange-correlation part, it lacks absolute accuracy in doing so. Instead of completely dismissing this method and adopting an entirely new approach like self-consistent GW, making minor corrections within this existing framework might prove beneficial. So one can count on an effective single-particle potential $V^{xc}(\mathbf{r})$, which contains some of the exchange-correlation effects in a many-body system and approximates reasonably well the self-energy. Within this framework then, one can consider the solution of KS equation Eq. (2.8) as a first order approximation for quasiparticle equations Eq. (2.27). For instance, in the solution of

$$\hat{H}_{KS}(\mathbf{r})\phi_i(\mathbf{r}) = \epsilon_i\phi_i(\mathbf{r})$$

where $\phi's$ are KS orbitals, with

$$\hat{H}_{KS} = -\frac{1}{2}\nabla^2 + V_{ext}(\mathbf{r}) + V^H(\mathbf{r}) + V^{xc}(\mathbf{r}),$$

one can consider KS orbitals $\phi_i(\mathbf{r}) \equiv \psi_n(\mathbf{r})$ and their corresponding eigenvalues $\epsilon_i \equiv \mathbb{R}(\epsilon_n)$ as a solution of quasiparticle equation:

$$\Big[-\frac{1}{2}\nabla^2 + V_{ext}(\mathbf{r}) + V^H(\mathbf{r}) + V^{xc}(\mathbf{r})\Big]\psi_n(\mathbf{r}) + \int d\mathbf{r}'\Delta\Sigma(\mathbf{r},\mathbf{r}';\epsilon_n)\psi_n(\mathbf{r}') = \epsilon_n\psi_n(\mathbf{r}). \quad (2.31)$$

This equation is similar to Eq. (2.27), where,

$$\Delta\Sigma(\mathbf{r},\mathbf{r}';\epsilon_n) = \Sigma(\mathbf{r},\mathbf{r}';\epsilon_n) - V^{xc}(\mathbf{r}')\delta(\mathbf{r}-\mathbf{r}')$$

is called quasiparticle correction. Since we assume that V^{xc} takes care of most of the correlation part, therefore we can treat quasiparticle correction $\Delta\Sigma$ as small and can treat it using first order perturbation to KS eigen values:

$$\epsilon_i^{qp} = \epsilon_i + \langle\psi_i(\mathbf{r}_1)|\mathbb{R}[\Delta\Sigma(\mathbf{r}_1,\mathbf{r}_2;\epsilon_i^{qp})]|\psi_i(\mathbf{r}_2)\rangle\,. \tag{2.32}$$

The self energy Σ is calculated in terms of screened Coulomb potential [42], given by the following expression:

$$\Sigma(\mathbf{r},\mathbf{r}';\epsilon) = \frac{\iota}{2\pi}\int G_0(\mathbf{r},\mathbf{r}';\epsilon+\epsilon')W_0(\mathbf{r}',\mathbf{r};\epsilon') \tag{2.33}$$

where

$$G_0(\mathbf{r},\mathbf{r}';\epsilon) = \sum_{\mathbf{k}}\frac{\psi_k(\mathbf{r})\psi_k(\mathbf{r}^*)}{\omega-\tilde{\epsilon}_k} \tag{2.34}$$

with $\tilde{\epsilon}_{\mathbf{k}} = \epsilon_{\mathbf{k}} + \iota\eta sgn(\epsilon_F - \epsilon_{n\mathbf{k}})$, ϵ_F being fermi-energy. The dynamically screened Coulomb potential $W_0(\mathbf{r},\mathbf{r}';\epsilon)$ is given by

$$W_0(\mathbf{r},\mathbf{r}';\epsilon) = \int \varepsilon^{-1}(\mathbf{r},\mathbf{r}_1;\epsilon)v(\mathbf{r}_1,\mathbf{r}')d\mathbf{r}_1 \tag{2.35}$$

where $\varepsilon(\mathbf{r},\mathbf{r}';\epsilon)$ is a dielectric function calculated as

$$\varepsilon(\mathbf{r},\mathbf{r}';\epsilon) = \delta(\mathbf{r},\mathbf{r}') - \int v(\mathbf{r},\mathbf{r}_1)P_0(\mathbf{r}_1,\mathbf{r}';\epsilon)d\mathbf{r}_1 \tag{2.36}$$

$P_0(\mathbf{r}_1,\mathbf{r}';\epsilon)$ is the polarizability computed according to

$$P_0(\mathbf{r}_1,\mathbf{r}';\epsilon) = -\frac{1}{2\pi}\int G_0(\mathbf{r},\mathbf{r}';\epsilon+\epsilon')G_0(\mathbf{r},\mathbf{r}';\epsilon')e^{\iota\omega'\eta}d\omega' \tag{2.37}$$

where η is a small positive real number. The first application of this method was carried out by Hybertsen and Louie in 1985 [44]. Subsequently, numerous papers [45, 46] emerged employing this approach to predict the properties of various materials, closely aligning with experimental observations to a significant extent.

2.2.4 Implementation of G_0W_0 in exciting

The implementation of G_0W_0 utilizes an auxiliary mixed product basis [47], that offers a highly flexible representation of various physical properties, including polarizability, the dielectric function, and other nonlocal quantities [48]. The usage of Mixed basis (MB) allows us to convert the equations Eq. (2.34) and Eq. (2.36) into a computationally tractable matrix form. As discussed in the last section, `exciting` is based on Linear Augmented Plane Waves basis function. The LAPW function is comprised of two components, one for the Muffin Tin (MT) region and other for the Interstitial ($\mathbb{I}$) region. In order to represent products of two Kohn–Sham wavefunctions accurately, a basis with similar features should be used. The MB consists of spherical harmonics and plane waves within MT's and $\mathbb{I}$, respectively. An optimal set of these MB functions, $\chi_i^q(r)$, accurately represents a product of two KS wave functions such as

$$\phi_{\mathbf{k}}(\mathbf{r})\phi^*_{\mathbf{k}-\mathbf{q}}(\mathbf{r}) = \sum_i M^i(\mathbf{k},\mathbf{q})\chi_i^{\mathbf{q}}(\mathbf{r}), \tag{2.38}$$

where $M^i s$ are the expansion coefficients and $\mathbf{q} = \mathbf{k} - \mathbf{k}'$. The quality of the mixed basis is determined by two main parameters: L_{MB} determines the angular momentum for the spherical-harmonics expansion, while G_{MB} determines the number of plane waves based on the cutoff parameter. Details on the construction and implementation of orthonormal mixed basis can be found in [47]. Apart from the quality of MB, the number of empty states, size of $\mathbf{k}$ and $\mathbf{q}$ grids, and the number of frequencies used to represent the correlation self-energy and to calculate the convolution integral, Eq. (2.33), are the most important computational parameters. The workflow for the $G_0 W_0$ implementation in `exciting` is given in the figure 2.3.

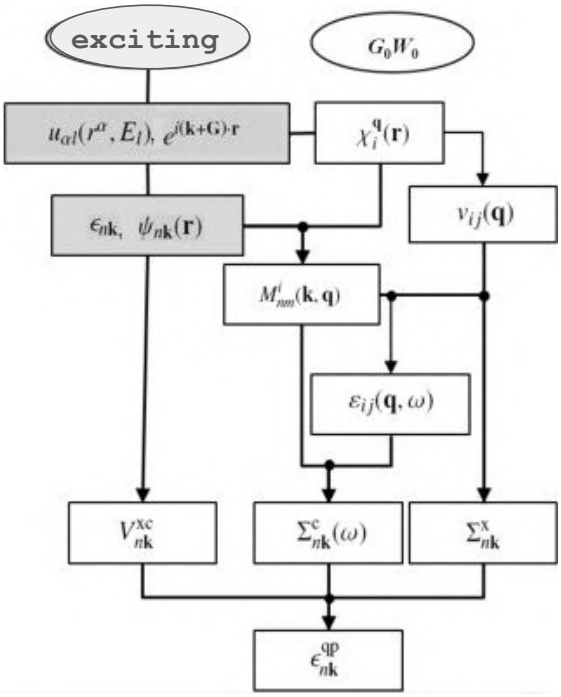

Fig. 2.3: Workflow of $G_0 W_0$ implementation in `exciting` [47]. The gray boxes indicate quantities obtained from the ground-state calculation.

Coulomb Truncation

In calculations involving periodic boundary conditions for 2D systems, a significant amount of vacuum is necessary to prevent spurious interactions between the replicas along the out-of-plane direction. Asymptotic decay is observed in both local and semi-local functionals, which is faster than $1/r$, aiding in the rapid convergence of unoccupied states and Kohn-Sham (KS) gaps with respect to vaccum size. However, in the case of $G_0 W_0$ calculations, the $1/r$ decay of the self-energy term significantly slows down the entire computation. To mitigate this issue, we employ a step function to truncate this potential along the out-of-plane direction z. This leads to a well-converged $G_0 W_0$ band gaps with a considerably smaller vacuum size [11, 49]. The truncation is done using a step function along z direction by setting the cutoff length of $L/2$, where L is the size of the supercell along z. The truncated Coulomb potential can be written in a planewave

basis as [50]:

$$v_{GG'} = \delta_{GG'} \frac{4\pi}{Q^2}[1 - \exp -Q_{xy}L/2 \cos G_z L/2], \tag{2.39}$$

where $\mathbf{Q} = \mathbf{q} + \mathbf{G}$ is a vector in first Brillouin zone.

$\mathbf{q} = \mathbf{0}$ treatment

By truncating the Coulomb potential, on one hand we benefit in achieving more accuracy in $G_0 W_0$ calculation while on the other it leads to slow convergence in terms of k-points. The slow convergence is mainly due to the non-smooth behavior of the dielectric function around the singularity at $\mathbf{q} = \mathbf{0}$ [11, 51, 52]. To circumvent this issue, it becomes necessary to analytically treat W^c ($W^c = W_0 - v(\mathbf{r}, \mathbf{r}')$) near this singularity, as proposed in [11, 51]. In the absence of this treatment the expression of Σ_c is given by [47]:

$$\langle \Psi | \Sigma_c | \Psi \rangle = \frac{\iota}{2\pi} \sum_{mij} \int_{-\infty}^{\infty} d\omega' \frac{1}{\mathbf{N_q}} \sum_{q} \frac{1}{\omega + \omega' - \tilde{\epsilon}_{m\mathbf{k}-\mathbf{q}}} [M^i_{nm}(\mathbf{k}, \mathbf{q})]^* M^j_{nm}(\mathbf{k}, \mathbf{q}) W^c_{ij}(\mathbf{q}, \omega'), \tag{2.40}$$

Now in order to treat this expression near singularity one needs to replace the integrand by,

$$\frac{1}{\omega + \omega' - \tilde{\epsilon}_{m\mathbf{k}}} [M^i_{nm}(\mathbf{k}, \mathbf{0})]^* M^j_{nm}(\mathbf{k}, \mathbf{0}) \frac{1}{\Omega_0} \int_{\Omega_0} d\mathbf{q} W^c_{ij}(\mathbf{q}, \omega'), \tag{2.41}$$

where Ω_0 is a small region around $\mathbf{q} = \mathbf{0}$ and we apply analytical expression of $W^c_{ij}(\mathbf{q}, \omega')$ in the limit $\mathbf{q} \to \mathbf{0}$ [11, 51] to evaluate the integral.

Chapter 3

Methodology

3.1 Geometry

First-principles calculations have been carried out for 3 materials: MoS_2, Au, and the heterostructure MoS_2 and Au (from now on represented by Au_x/MoS_2). For MoS_2 monolayer, the geometry has been optimized with the *Perdew-Burke-Ernzerhof (PBE)* functional, giving rise to a lattice parameter of a = 3.19 Å, and distance between sulfur-sulfur atom (d_{SS})=3.15 Å. Figure(3.1) illustrates the lateral view of MoS_2 super cell which is used in the DFT calculation.

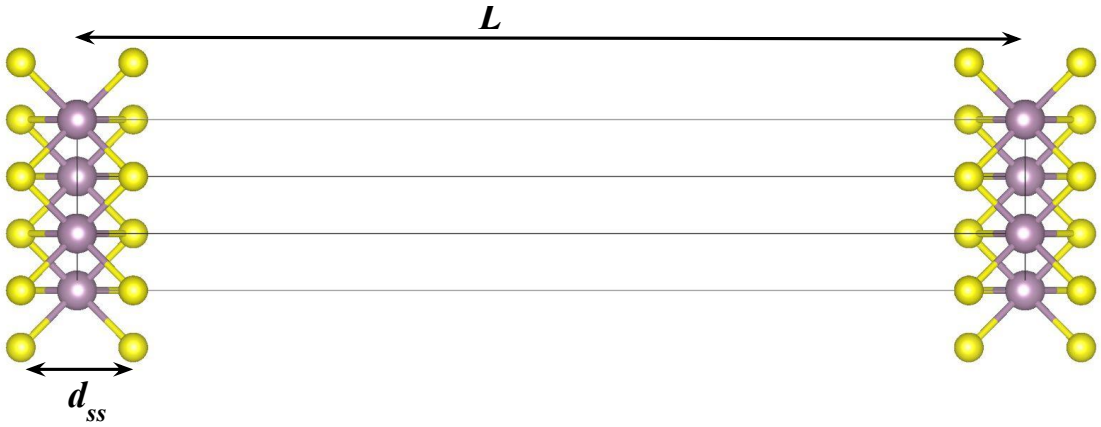

Fig. 3.1: MoS_2 unit cell

For the heterostructure Au_x/MoS_2 we opted for the matched models of 1×1 unit cell of MoS_2 on a 1×1 unit cell of Au in three different geometries *i.e.* FCC, HCP and on-top, as shown in the top panel of figure 3.2a. This approach is computationally economical as it only requires maintenance of single unit cell. The three different matched models were selected based on the relative positioning of the MoS_2 monolayer with respect to the underlying substrate. These models encompass three distinct S-Au contact regions, which aligns closely with the pertinent characteristics observed in the experimental setup. Consequently, the combination of these three matched models closely approximates the experimental configuration—which otherwise is achievable solely through mismatched models. This strategic approach reduces the system size

considerably without deviating much from the experimental setup. The bottom panel of figure 3.2a shows the top view of the mismatched model used for calculation by Bruix *et al.* [53]. It consists of a $\sqrt{13} \times \sqrt{13}R13.9°$ MoS_2 cell on a 4×4 Au cell. This model comes, however, with an increased computational cost, since the number of atoms in such mismatched cell can be quite high.

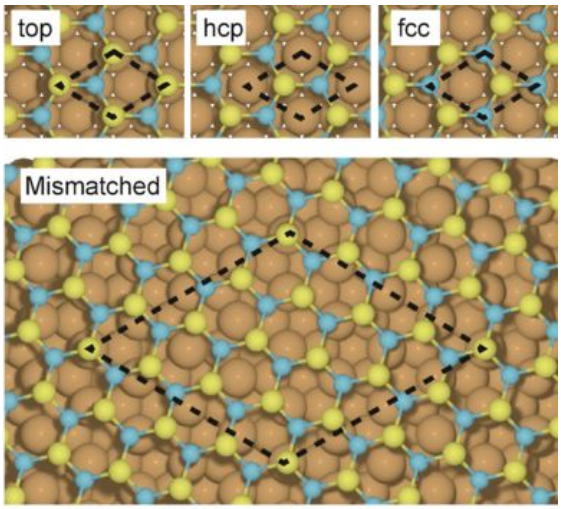

(a) The different positions considered of the bottom S atoms with respect to the underlying Au lattice (on-top, hcp, and fcc). Top view (middle panel) of mismatched model [53].

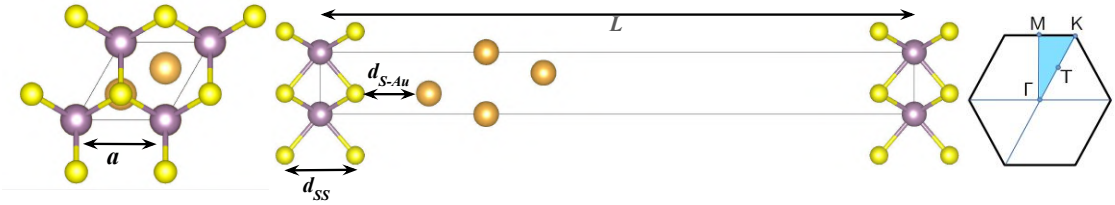

(b) Top and side view of Au_3/MoS_2 slab geometry, determined by plane lattice constant a and distance between sulfur atoms, d_{SS} with $d_{S-Au} = 3.29$ Å. High symmetry points and path used to draw band structure (right panel) [11].

Fig. 3.2

The electronic properties of MoS_2 are significantly influenced by its surroundings. Both the composition of the substrate and the thickness of its layers significantly contribute in determining its properties. To discern the effects arising from the thickness of the substrate, we systematically increased the number of gold layers in the heterostructure Au_x/MoS_2 to $x =$ 3, 6, and 9. Figure 3.2b illustrates the top and side views of the on-top model for one such heterostructure, Au_3/MoS_2. In this model, the geometry of MoS_2 is kept fixed as determined by its free-standing counterpart, and the distance of the gold layers is maintained at a constant distance of $d_{S-Au} = 3.29$ Å, which is equal to the optimized distance for the mismatched model [53]. The unit-cell size L along the out-of-plane direction is chosen so that the distance between the first sulfur atom and the last gold atom remains constant, as shown in table 3.1.

Table 3.1: Unit cell length(L) and `rgkmax` for different structures of Au+MoS_2

	MoS_2	Au_3	Au_3MoS_2	Au_6MoS_2	Au_9MoS_2
L in Å	26.58	26.58	26.58	34.76	41.97
`rgkmax`	8	11.51	8.0	8.0	8.0

3.2 Lattice Mismatch

The lattice constants of materials describe the spacing of atoms in the system. Contacting two materials with different lattice constants creates a boundary region where two crystal structures meet. If there is a significant difference in the lattice constants, it leads to artificial strain at the interface, rendering the system incommensurable. In electronic structure calculations, it is necessary to use commensurate structures to model incommensurate systems. The study by Farmanbar *et. al.* [54] has shown that the binding energies between MoS_2 and Au at the equilibrium distance $d_{eq} = 2.6$ Å are much smaller than those needed for true chemical bonding. With such a weak *metal/adsorbate* interaction, it is unlikely that the metal substrate can impose its lattice periodicity onto the MoS_2 overlayer. Therefore, the metal/MoS_2 interface is very likely to become incommensurable if the lattice mismatch is substantial.

If we want a comparable structure, we need to obtain a significantly larger supercell, as shown in the bottom panel of Figure 3.2a. Performing DFT calculations on such a large supercell may be feasible for a single instance, but for G_0W_0calculations, this system becomes considerably impractical. Hence, we have subdivided this large cell into three smaller parts: fcc, hcp, and top, as illustrated in the top panel of the same figure. These smaller parts constitute 1×1 unit cells of gold and have been arranged according to the relative positions of MoS_2. To achieve these compatible structures, we need to significantly modify the lattice parameters of any one of the subsystems. However, modifying the in-plane lattice constant of a monolayer significantly affects the electronic properties of the material. While modifying the lattice parameters of a metal surface by a few percent only mildly affects the electronic properties. Therefore, we adjusted the parameters of Au to achieve a commensurable system and adhered to the selection of a matched model, which is computationally efficient and involves maintaining a single cell.

3.3 Computational details

The DFT calculations are carried out employing a k-mesh grid of $30 \times 30 \times 1$ using the local density approximation (LDA) as exchange-correlation (xc) functional. Our calculations employ the linearized augmented plane wave + local orbital (LAPW+lo) basis as implemented in `exciting` code. The dimensionless parameter, `rgkmax`, which specifies the energy cutoff for the plane-wave basis set in `exciting` is set to 8 for MoS_2 and all the heterostructures of type MoS_2/Au. However, for the calculation with Au alone this parameter is set to 11.51. This is done in order to be consistent with the number of plane-waves used in the basis set.

In order to treat correlation part of calculation more efficiently, we augmented our DFT calculation with quasi-particle correction using the state-of-the-art G_0W_0 approach. The quasi-particle energies within the G_0W_0 approximation are given as a solution of the linearized QP Eq. (**??**). The number of the empty states, the size of q grids, and the number of frequencies used to represent the correlation self-energy are the most important computational parameter [55]. In our calculation we employed a q-mesh grid of $18 \times 18 \times 1$ along with 400 empty states. The

correlation part of self energy is evaluated with 32 frequency points along the imaginary axis, and then analytic continuation to the real axis is carried out by means of Pade's approximation. For the bare coulomb potential, we use a 2D cutoff [50] combined with a special treatment of the $q = 0$ singularity [51].

Chapter 4

Results and Discussion

4.1 DFT

Density Functional Theory calculations based on LDA xc-functional is carried out for gold, MoS_2, and the three heterostructures of type Au_x/MoS_2, where $x = 3, 6$ and 9. The following section presents a comparative study of the electronic properties of pristine layers of Au and MoS_2 with the heterostructure Au_x/MoS_2. Metallic substrate presents a significant challenge in achieving high device performance. This challenge often arises due to Fermi-level pinning when using high work function metals such as copper (Cu), aluminum (Al), gold (Au), and platinum (Pt) [56]. As a result of this pinning, a significant change in band dispersion is observed. This section provides a detailed assessment of the impact of Au substrate on 2D MoS_2.

4.1.1 Pristine MoS_2 and Au

Figure 4.1a depicts the band structure and Density of States (DOS) of pristine MoS_2 monolayer. The band structure is drawn along the k-path $\Gamma - M - K - \Gamma$, as shown in figure 4.1b. Upon examination of the band structure, it is evident that the MoS_2 in its monolayer form is semiconductor in nature with a direct band gap of 1.68 eV, which is situated at the K-point. The plot of DOS further confirms this observation.

Studies conducted on the band gap analysis of monolayer MoS_2 have reported different values for the fundamental band gap at the K point. However, they consistently found it to be of a direct nature. The experimental data from pump/probe angle-resolved photoemission spectroscopy found the band gap to be 1.95 ± 0.05 eV [57]. Another experiment using the Scanning Tunneling Spectroscopy technique obtained a band gap of 1.75 ± 0.27 eV [53]. Additionally, many studies utilizing first-principle calculations have reported the fundamental band gap to be approximately 1.8-1.9 eV [53, 54].

The significant variations in band gap values can be attributed to the high sensitivity of monolayer MoS_2 properties to structural parameters. These properties depend not only on the lattice constant but also upon the distance between sulfur-sulfur atoms (d_{SS}) [11], and unfortunately several studies only report lattice parameters not the d_{SS}. These geometrical differences primarily account for the considerable deviation in the band gap. Additionally, due to the strong exciton binding energies of monolayer MoS_2, the optical response is significant even at room temperature [9]. Experiments using ARPES and STS do not take this effect into consideration.

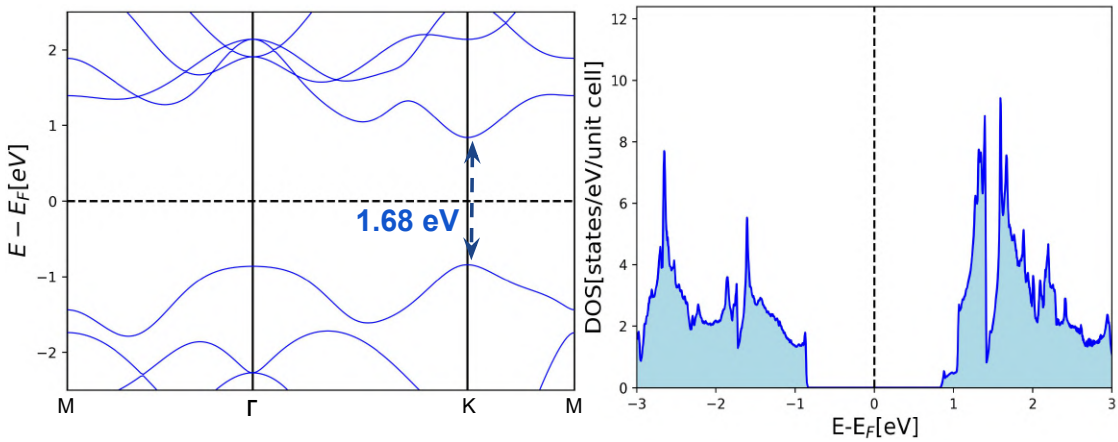

(a) DOS(right) and Band structure, along the k-path M − Γ − K − M, of freestanding MoS_2

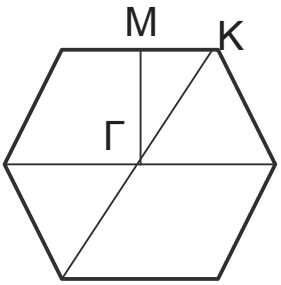

(b) k-path M − Γ − K − M

As a result, the experimentally reported values are lower than the one computed theoretically. However, a study by Klots *et al.* [9] using photo-current spectroscopy has demonstrated an extremely large binding energy for band-edge excitons, resulting in a band gap of 2.5 eV. A similar result is also demonstrated by our research group [11] in which they utilized the G_0W_0 method and found the band gap value of 2.5 eV.

Figure 4.2 illustrates the band structure and DOS of a system of 3 gold layers. DFT at the level of LDA is able to capture the true nature of the material i.e. metallic. The DOS is flat above the fermi level showing the behaviour observed by 2D systems [58]. The Density of States in 2D systems is constant because the energy increases quadratically in reciprocal space, which cancels out the areal density of points. This is not the case for 1D and 3D systems, where the energy increases linearly and cubically.

4.1.2 Heterostructure

Establishing electrical contact with 2D TMDCs significantly alters the band dispersion of the monolayer. Figure 4.3 illustrates the band structure of Au_3/MoS_2 projected onto MoS_2 and Au for three different geometries. The projection is displayed as a heat map plot, with the blue color indicating the projection of bands on the MoS_2, and the yellow color representing the projection on 3 layers of Au. From the figure, it is evident that the band dispersion around the Γ point in the energy range of $2-3$ eV is predominantly contributed by pristine MoS_2. However, significant band mixing is observed around the same point near fermi energy. Surprisingly, upon comparing

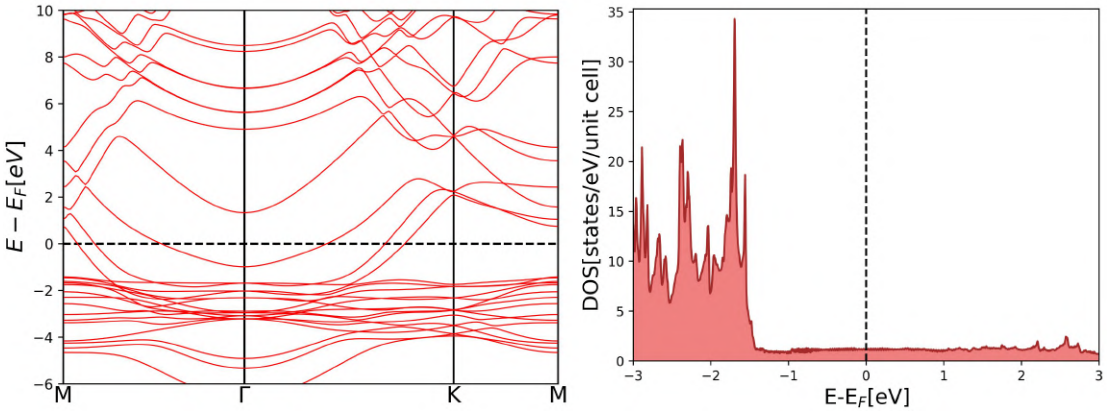

Fig. 4.2: Band structure(left) and DOS(right) first three gold (Au) layer along the k-path M − Γ − K − M

the band gap at the K point across all three structures, we found that the difference is quite negligible, only around 25 meV.

In order to better comprehend our system, we conducted the DOS analysis for all the three geometries, as shown in Figure 4.4. Here, the blue curve represents the density of states of the combined system, i.e. Au_3/MoS_2. However, the red plot shows the projection onto the MoS_2 monolayer. A comparative study comparing the DOS of their respective freestanding counterparts reveals that the discernible peaks above the fermi level in the combined DOS plot predominantly originate from MoS_2. However, a small peak near the fermi level emerges within the band gap of MoS_2 across all three structures. This peak is more prominent and distinct in the face-centered cubic (FCC) geometry. Notably, this peak does not correspond to any of the pristine counterparts.

This anomaly in the band structure and DOS motivates us to further investigate the band character with higher level of theory. Band gap underestimation is a well-known shortcoming of the LDA and GGA approaches. This issue can be partially addressed by incorporating a fraction of Hartree-Fock exchange, leading to the hybrid functional formalism, or by applying quasi-particle correction on top of DFT. Calculations using such techniques result in improved band gaps. In this project, we have augmented our DFT results by incorporating state-of-the-art G_0W_0 calculation.

The appearance of a peak in the band gap region of MoS_2 signifies that there is some form of bonding occurring between the substrate and monolayer. To ascertain this, we conducted a projection of the Density of States onto individual atoms. Figure 4.5, illustrates the same. The dashed red curve shows projection on 3 Au atoms, blue solid line is for Mo atom, S-up and

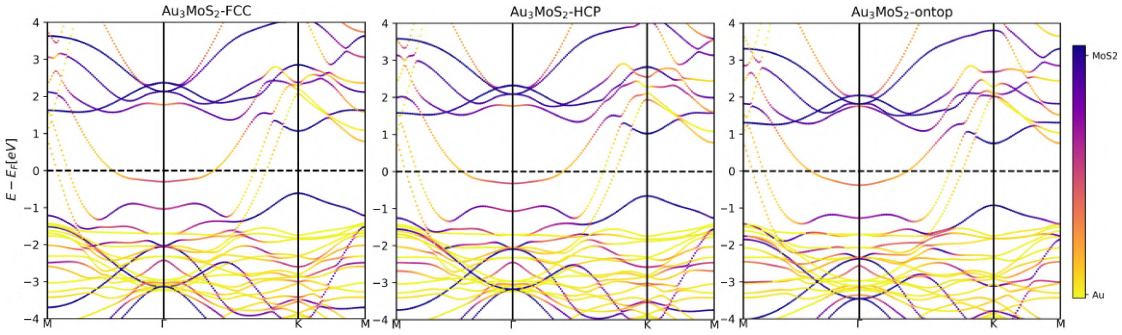

Fig. 4.3: Heat map plot of calculated band structure of $Au_3/MoS2$ with projection on Au(Yellow) and MoS_2(Blue)

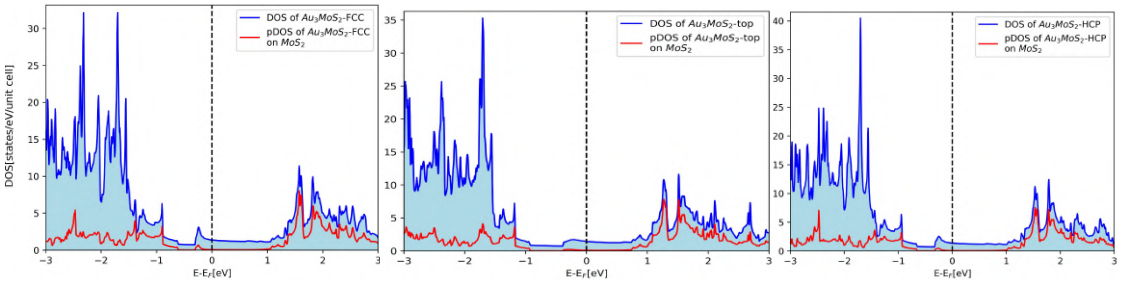

Fig. 4.4: Density of States(DOS) of $Au_3/MoS2$

down are represented by yellow and maroon solid lines respectively. The nomenclature, *S-up* and *S-down* is given with respect to the position of S-atom with respect to gold layer. The one lying close to the substrate is denoted by *S-down/bottom* and the other is called *S-up/top* as shown in figure 4.6. From the figure it is clear that out of all the atoms, the contribution from *S-down* is significant in formation of the peak in the intermediate region. This can be considered as a signature of bond formation between S atom and Au monolayer.

However, in order to further strengthen this claim, we evaluated the band structure projection onto the orbitals of each atom. Figure 4.7 illustrates the projection of bands onto valance orbitals of different atoms in the unit cell. The VBM at Γ shows significant contribution coming from the

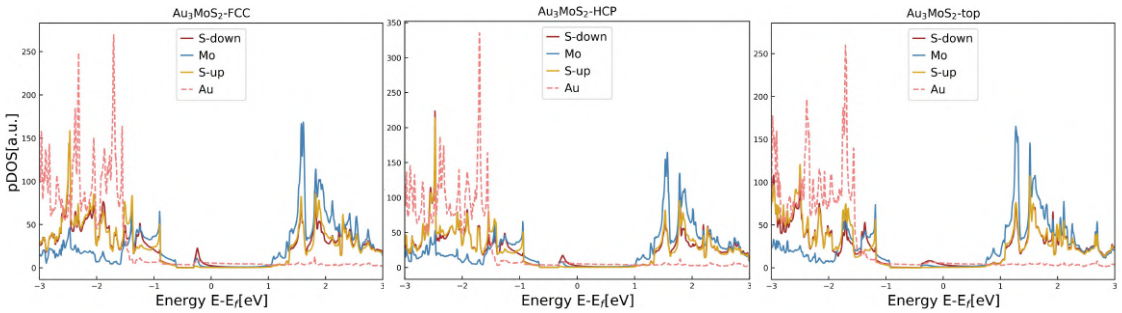

Fig. 4.5: Density of state of Au_3/MoS_2 projected upon each atom.

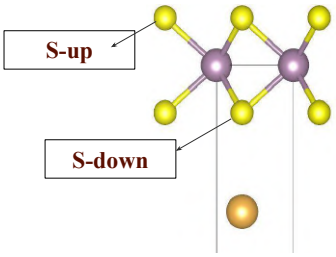

Fig. 4.6: S-up/top and S-bottom/down

out of plane orbitals of sulfur (S-*top*) $3p_z$ and Mo $4d_{z^2} + 4d_{yz}$, as shown in figure 4.7b, 4.7c. Notably, there is a pronounced asymmetry observed between top and bottom *p-orbitals* of S atom. The top sulfur $p - orbital$ participates with Mo d to form valence band states, depicting the band character of pristine MoS_2. However, the $3p_z$ orbital of bottom S atom seems to hybridize and merge with the Au $4d$, indicating the formation of $Au - S$ bond. This observation thus strengthens the above claim and confirms that the peak observed within the band gap region of the heterostructure Au_3/MoS_2 can be attributable to the interaction between *S-bottom* and *Au*.

The study of binding energy E_b (eV) per MoS_2 versus the equilibrium bonding distance d_{eq} for MoS_2 adsorbed on metal(111) [54], reveals that the distance for the gold layer to effectively bind the substrate is around 2.8 Å. See figure 4.8 for reference. Thus, it is not expected for Au layers to undergo chemisorption beyond this distance. The system we are studying is at an equilibrium distance of 3.29 Å above the Au layers. Even now, we are observing some interaction between the two systems. A separate study conducted by *P. Khakbaz et. al.* [19], however, claims that it is possible to observe such discernible peaks inside the band gap of MoS_2 even when the distance between the substrate and the monolayer is around ~ 4 Å . These peaks, referred to as *Intermediate Gap States (IGS)*, emerges as a consequence of charge transfer interactions between the monolayer and the substrate.

Figure 4.9, illustrates this charge transfer by analyzing the variation in charge density difference (Δn) along the direction of unit cell. This difference is derived by subtracting the individual system from the complete unit heterostructure, as shown in the following figure. Within this figure, an observable trend emerges wherein the charge density diminishes toward the S region, displaying a peak negativity, while conversely, it increases positively toward the Au side. This observation corroborates the inference that there is a diminution of charge in the S region, concurrently accumulating in the region of gold. Thus, it can be distinctly stated that there is a transfer of charge occurring between gold and sulfur. However, the magnitude of this charge transfer is very less in magnitude, suggesting that it does not align with the direction of a chemical bond or chemisorption.

4.1.3 More Layers

It is generally accepted that the substrate alters the photophysical properties of ultrathin TMDs via the following mechanisms: strain, dielectric screening, charge transfer, and optical interference effects [59–61]. The magnitude of these effects depends on both the nature of substrate and its thicknesses. During the latter phase of the project, we conducted an analysis concerning the impact of substrate thickness on monolayer MoS_2. While keeping the monolayer fixed, we increased the number of layers of gold. Figure 4.10 represents the band structure for three

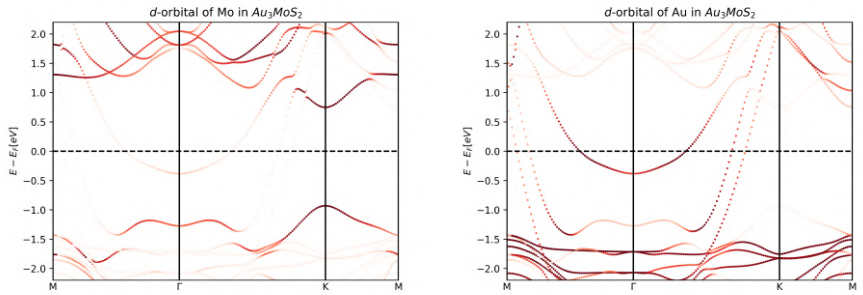

(a) Mo *d-orbital* (b) Au *d-orbital*

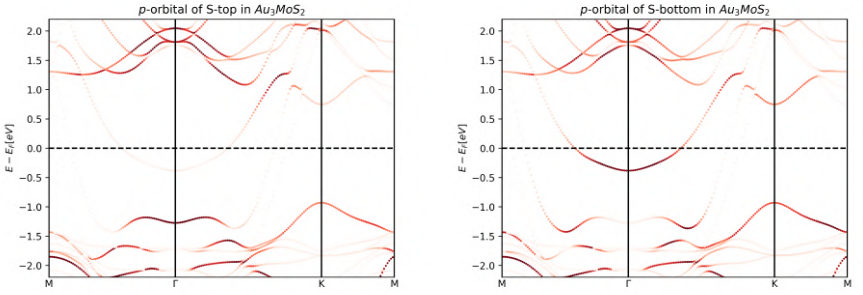

(c) S-top *p-orbital* (d) S-bottom *p-orbital*

Fig. 4.7: Orbital projected band structure of Au_3MoS_2

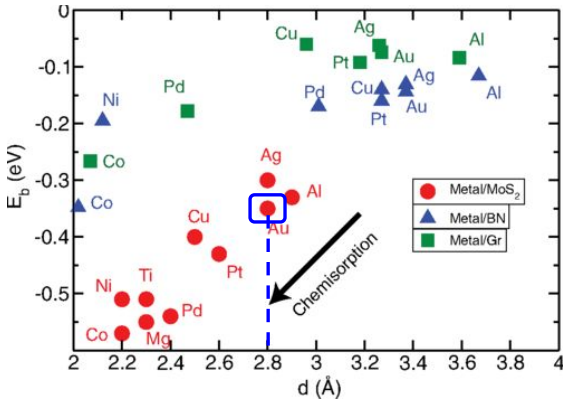

Fig. 4.8: Binding energy E_b (eV) per MoS_2 versus equilibrium bonding distance d_{eq} Åfor MoS_2 upon different substrates, taken from [54]

different heterostructure Au_3/MoS_2, Au_6/MoS_2, and Au_9/MoS_2 projected onto MoS_2 and Au with the same colour scheme as before.

The analysis of the band structure reveals that as the number of gold layers increases, the gold bands gradually shift downward below the fermi level. Despite the increase in Au layers, there

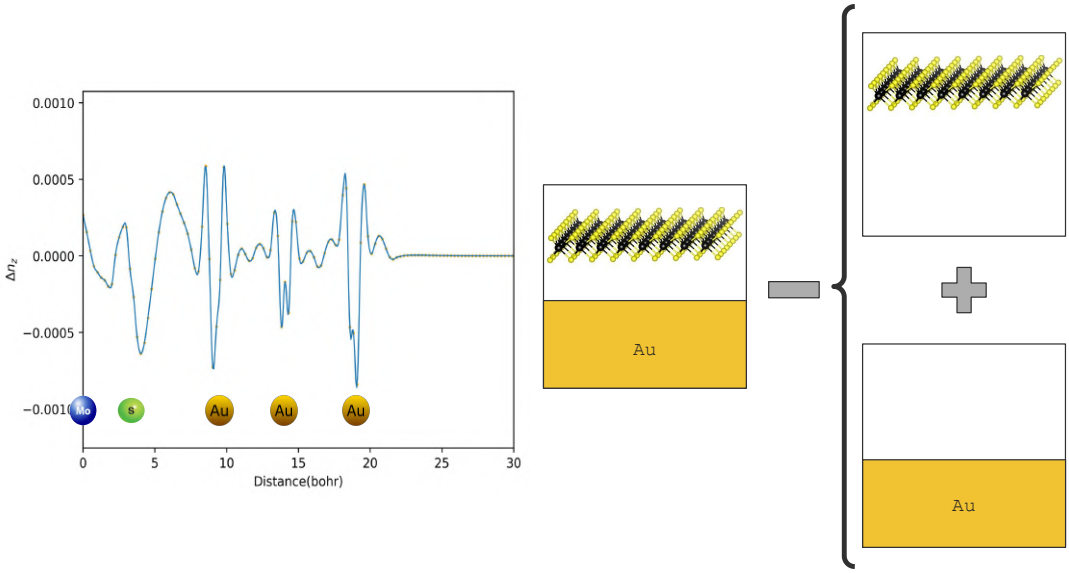

Fig. 4.9: The electron density difference $\Delta n(z)$ of MoS_2/Au interface at $d_{eq} = 3.29$Å(left panel) and the way this difference is calculated (right panel).

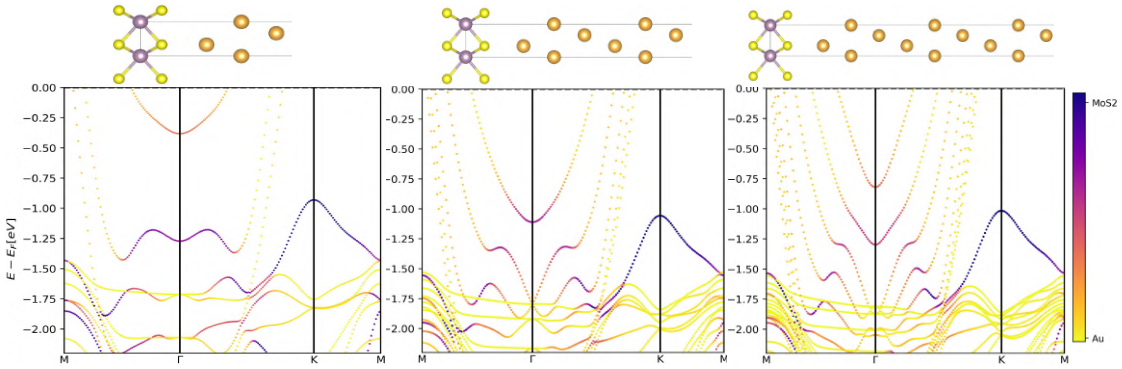

Fig. 4.10: Heat map plot of band structure for Au_3/MoS_2, Au_6/MoS_2, and Au_9/MoS_2.

was hardly any noticeable difference in the fundamental gap at K. Conversely, the contribution of Au to the bands near the Γ point in the vicinity of the fermi level increased. This can be attributed to the shift of Au bands due to increased number of layers. When we conducted a density of state plot and compared the results, we found them quite intriguing. Figure 4.11 represents the projected density of states for three heterostructures: red indicates 3 layers of gold (Au_3), cyan represents 6 Au layers (Au_6), and dashed red illustrates 9 gold layers (Au_9). Upon comparing these plots, we observed that the peak which was present in the case of 3 Au layers is now not visible in the cases of 6 and 9 Au layers. From this, we deduced that 3 Au layers are insufficient to properly converge the calculation, hence necessitating the use of at least 6 layers.

This can be comprehended as follows: in the case of 3 Au layers, surface atoms possess some

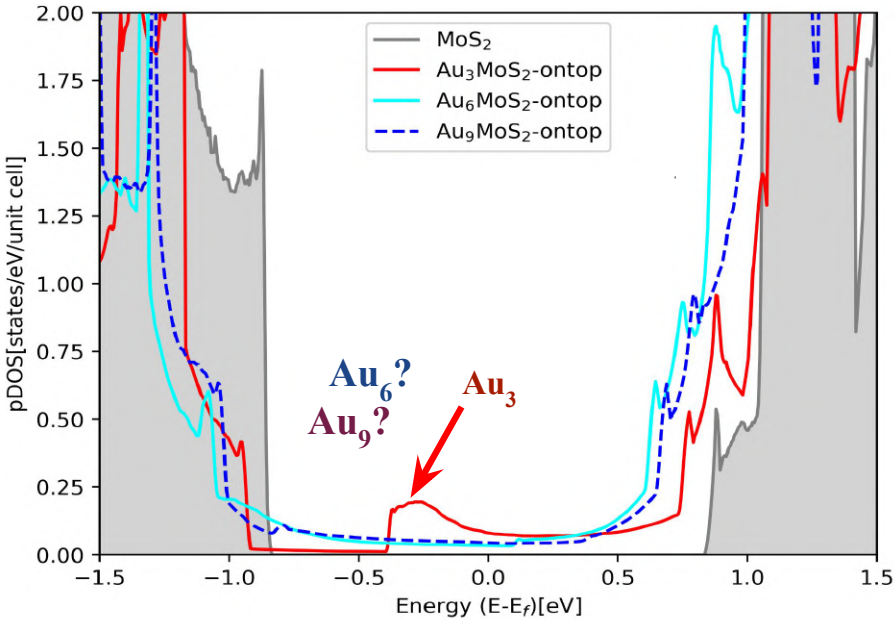

Fig. 4.11: Density of State Projected on MoS_2 for 3 different heterostructures

unbound bonds known as dangling bonds. These dangling bonds redistribute their electron cloud by bonding with adjacent layers, either above or below. With only 3 Au layers, the surface atoms lacked sufficient neighboring Au atoms to share their dangling bond's electron cloud. Therefore, in the scenario of Au_3MoS_2, the next nearest atom, happens to be S, which shared its electron cloud with the surface Au atom. Consequently, the phenomenon of charge transfer was observed in that case. However, as we increased the number of layers, each Au atom has sufficient neighboring Au atoms to fulfill the requirements of its dangling bonds.

4.2 $G_0 W_0$

The DFT calculations provide us with a good qualitative understanding of the nature of MoS_2. Through its application, we have achieved considerable success in elucidating various aspects MoS_2 and substrate interaction, like band mixing at Γ point, charge transfer between monolayer and substrate etc. However, the band gap values obtained from experimental data [9] do not align with our theoretical calculations. Additionally, DFT's LDA and GGA functionals are quite unpopular in accurately predicting band gaps [40]. Consequently, a need for corrections to our DFT-derived results arises.

To address this issue, corrections can be made by improving the functionals, incorporating additional parameters such as Hubbard parameters, or utilizing Hybrid functionals. Nevertheless, we intend to employ the state-of-the-art $G_0 W_0$ method to enhance the accuracy of our results, as discussed in the subsequent section. Due to time constraints, we do not have sufficient data to perform detailed analysis. Therefore, our discussion will focus on the available results.

4.2.1 Pristine MoS_2

Figure 4.12 illustrates the band structure and density of states of pristine MoS_2. The red-colored plot represents the G_0W_0 calculation, while the blue-colored plot corresponds to the $KS-DFT$ calculation. By examining the band structure, it is evident that the G_0W_0 calculation has not only altered the direct band gap at the K point, increasing it from 1.68 eV to 2.59 eV but has also transformed the nature of fundamental gap from direct band gap at K to indirect band gap of **2.55 eV** between K and T points. The DOS plot exhibits a similar trend, showing an increased gap of MoS_2 after the application of the G_0W_0 method.

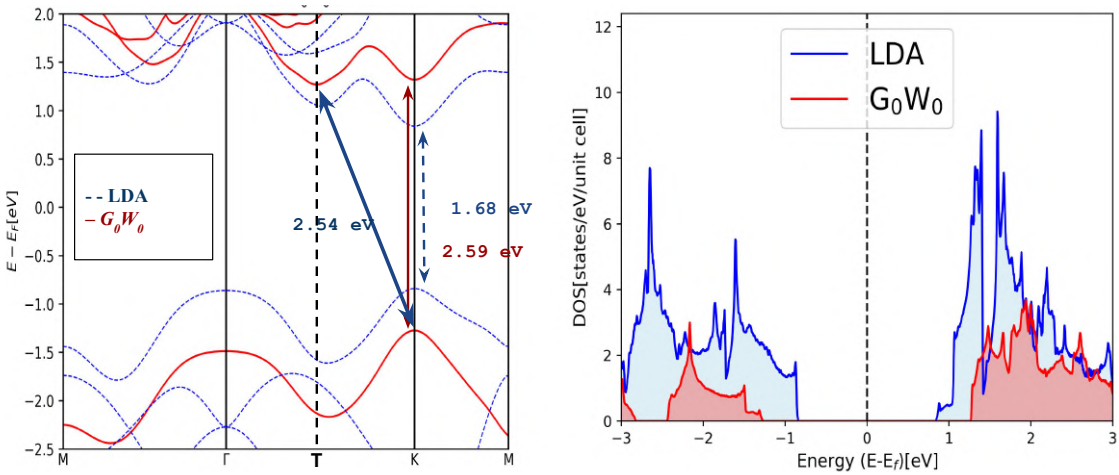

Fig. 4.12: Band structure and Density of state of pristine MoS_2 calculated through G_0W_0 (red) and LDA (blue)

The experimental band gap for free-standing MoS_2, as determined by photocurrent spectroscopy, is 2.5 eV [9]. In order to compare with the experiment, it is important to consider the zero-point renormalization energy of 75 meV [62]. This means that the theoretical value computed without this correction should be $2.55 \pm 0.075 \approx 2.6$ eV to align with its measured counterpart. Although our G_0W_0 calculation aligns well with the experiment, it wrongly predicts an indirect band gap that is 44 meV smaller than the direct gap at the $K-K$ point. The study conducted by [11] encountered the same issue. However, it has been demonstrated that using the G_0W_0 calculations on top of DFT with PBE functional resolves this issue. Also, the results obtained using PBE functional closely aligns with experimental observation. In our study we stick to LDA functional, acknowledging that the PBE provides an accurate description of the band gap and can be used when required.

4.2.2 Heterostructure

The DFT calculation have revealed that contacting Au layers with a MoS_2 leads to noticeable changes in the band structure. However, despite this, no alterations are observed in the fundamental gap, as shown in FIg. 3.2. One possible explanation for this discrepancy could be the inadequate consideration of correlation in DFT LDA functional, resulting in the ineffective portrayal of substrate screening. In this section, we address this issue through G_0W_0 calculations.

Due to time constraints, the G_0W_0 calculations for the optimal $18 \times 18 \times 1$ q-mesh could not be completed. Consequently, we conducted an analysis using a smaller q-mesh grid. For G_0W_0 calculation we are only considering Au_3/MoS_2 due to computational limitations.

Table 4.1: G_0W_0 band gap of Au_3/MoS_2 for two different q-mesh

q-mesh	$K - K$ Band-gap [eV]
$6 \times 6 \times 1$	2.68057
$9 \times 9 \times 1$	2.18235

Table 4.1 illustrates the direct band gap measurement at the K-point, $E_g(K - K)$, for two different q-mesh grids: $6 \times 6 \times 1$ and $9 \times 9 \times 1$, respectively. From this table, it is evident that increasing the q-sampling has led to a decrease in the value of the $E_g(K - K)$. The study by Pelá *et al.* [11] on pristine MoS_2 has shown that the $E_g(K - K)$ gap decreases as the q-mesh increases and gradually tends towards convergence. Additionally, their study has shown that when $q = 0$ treatment [51] is taken into account during G_0W_0 calculation, a q-mesh of $18 \times 18 \times 1$ yields results significantly close to a fully converged calculation.

In Table 4.1, it can be observed that the difference between the band gap $E_g(K - K)$ in going from $6 \times 6 \times 1$ to $9 \times 9 \times 1$ is ~ 0.5 eV, whereas in the case of pristine MoS_2, this difference is only 0.17 eV [11]. This clearly indicates that the band gap of the K point has been significantly influenced by the screening of the Au substrate. The gap, which experienced only a marginal change on the order of meV in DFT calculations, Sec. 4.1.2, now exhibits a considerable variation. Consequently, it is apparent that despite the $9 \times 9 \times 1$ calculation is not fully converged, the influence of Au is still discernible. Hence, to properly account for the screening effect of the metallic substrate, the application of the G_0W_0 approach becomes necessary.

4.2.3 Comparison with Experiment

Experimental study based on Angle Resolved Photo-emission Spectroscopy (ARPES) and AR-Inverse-PES (ARIPES) measurements at the K-point for MoS_2/Au heterostructure comes out to be 1.9 eV [63]. The band gap obtained in our calculation differs from their value because we have not accounted for the exciton binding energy and Spin Orbit Coupling. In order to accurately describe the band gap, it is necessary to perform BSE calculations on top of G_0W_0 level, incorporating the calculation of exciton binding energy. This exciton binding energy significantly reduces the band gap. The study of Park *et al.* [63] has demonstrated that the exciton binding energy for the MoS_2/Au heterostructure comes out to be 0.6 eV.

Sec. 4.2.1 has already talked about the zero point correction of 75 meV in the ground state calculation, and upon incorporating the effect of spin orbit coupling on top alters the gap by the order of 90 meV [11]. Here, we have supposed that the spin orbit splitting is independent of the presence of substrate. Thus, the overall QP band gap by reduces by ~ 0.4 eV giving the resultant gap of 1.75 eV.

At present, we only have these results available for the G_0W_0 calculations. Even these preliminary findings are capable of indicating the change in the fundamental gap of Au_3/MoS_2 which was not captured in DFT results. For a more detailed and concrete analysis, we are await-

ing the results for configurations of $12 \times 12 \times 1$, $15 \times 15 \times 1$, and $18 \times 18 \times 1$. Once these are completed, we will be able to refine our analysis further.

Chapter 5

Conclusion

The aim of this thesis is to investigate the impact of a metallic substrate, particularly gold, on the behavior of MoS_2. Due to the computational complexity of using the entire structure, the approach involved dividing it into three subsystems: fcc, hcp, and ontop, each containing one unit cell of gold.

The initial investigations focused on the electronic properties of pristine MoS_2 and gold separately using KS-DFT. This method provided a qualitative understanding of the system, revealing significant changes in the band structure at the Γ point when 3 layers of gold contacted MoS_2. However, minimal alteration was observed at the K point, where the fundamental gap exists, across all three geometries considered in the calculations.

Notably, the analysis of the density of states for the heterostructure revealed a small peak within the band gap, which was particularly prominent in the FCC geometry. Further examination through the analysis of projected DOS indicated an interaction between the S-bottom of MoS_2 and the adjacent gold layers, as supported by orbital projected band structures.

Although the distance between the gold layers and the $S - bottom$ is greater than the threshold required for chemisorption, charge density difference plots confirmed a depletion of charge near the S atom and accumulation near the gold. This affirms an interaction that influences the band structure. This interaction arises from the bonding tendencies of surface gold's dangling bonds with the nearest S atoms due to the insufficient availability of gold layers.

Increasing the number of layers mitigated the observed peak in the band gap region, as the gold atoms compensated for their electron clouds by interacting with adjacent layers, thereby reducing their influence on the band structure.

While the DFT calculations, even with the LDA functional, provided qualitative insights into the interaction, they underestimated the band gap due to the limitations in effectively accounting for correlations. The non-local effect of image charges induced by the gold substrate is not accounted for by the LDA functional due to its semi-local nature. This prompted the use of G_0W_0 calculations as a correction to the KS eigen equations.

The G_0W_0 correction on the q-mesh of $18 \times 18 \times 1$ improved the band gap estimation for the free-standing monolayer, transforming it from direct to indirect. This anomaly of changing

the nature of the band gap can be corrected by using more advanced functionals such as PBE. For the heterostructure, G_0W_0 analysis carried out on a q-mesh of $6 \times 6 \times 1$ and $9 \times 9 \times 1$ highlighted the substrate's impact on the band structure at the K point, demonstrating a decrease in the gap size due to screening. However, due to time and computational resource limitations, the calculation for the q-mesh $18 \times 18 \times 1$ could not be completed. Yet, preliminary results indicate that increasing the q-mesh resolution would provide closer approximations to the true values.

In summary, this study successfully explained the changes in the band gap due to substrate screening and suggested the need for further exploration of charge transfer phenomena with increased layer convergence. Subsequent analyses using larger q-meshes are still pending, offering the potential for deeper insights into the substrate's influence on MoS_2 behavior.

Bibliography

[1] K. S. Novoselov et al. "Electric Field Effect in Atomically Thin Carbon Films". In: *Science* 306.5696 (2004), pp. 666–669. DOI: 10.1126/science.1102896. eprint: https://www.science.org/doi/pdf/10.1126/science.1102896. URL: https://www.science.org/doi/abs/10.1126/science.1102896.

[2] A. H. Castro Neto et al. "The electronic properties of graphene". In: *Rev. Mod. Phys.* 81 (1 Jan. 2009), pp. 109–162. DOI: 10.1103/RevModPhys.81.109. URL: https://link.aps.org/doi/10.1103/RevModPhys.81.109.

[3] Merin Tomy et al. "Emergence of Novel 2D Materials for High-Performance Supercapacitor Electrode Applications: A Brief Review". In: *Energy & Fuels* 35.24 (2021), pp. 19881–19900. DOI: 10.1021/acs.energyfuels.1c02743. eprint: https://doi.org/10.1021/acs.energyfuels.1c02743. URL: https://doi.org/10.1021/acs.energyfuels.1c02743.

[4] Xidong Duan et al. "Two-dimensional transition metal dichalcogenides as atomically thin semiconductors: opportunities and challenges". In: *Chem. Soc. Rev.* 44 (24 2015), pp. 8859–8876. DOI: 10.1039/C5CS00507H. URL: http://dx.doi.org/10.1039/C5CS00507H.

[5] Xiaofei Zhou, Hainan Sun, and Xue Bai. "Two-Dimensional Transition Metal Dichalcogenides: Synthesis, Biomedical Applications and Biosafety Evaluation". In: *Frontiers in Bioengineering and Biotechnology* 8 (2020). ISSN: 2296-4185. DOI: 10.3389/fbioe.2020.00236. URL: https://www.frontiersin.org/articles/10.3389/fbioe.2020.00236.

[6] Manish Chhowalla et al. "The chemistry of two-dimensional layered transition metal dichalcogenide nanosheets". In: *Nature Chemistry* 5.4 (Apr. 2013), pp. 263–275. ISSN: 1755-4349. DOI: 10.1038/nchem.1589. URL: https://doi.org/10.1038/nchem.1589.

[7] Nikhitha Joseph, P. Muhammed Shafi, and A. Chandra Bose. "Recent Advances in 2D-MoS2 and its Composite Nanostructures for Supercapacitor Electrode Application". In: *Energy & Fuels* 34.6 (2020), pp. 6558–6597. DOI: 10.1021/acs.energyfuels.0c00430. eprint: https://doi.org/10.1021/acs.energyfuels.0c00430. URL: https://doi.org/10.1021/acs.energyfuels.0c00430.

[8] Vydha Pradeep Kumar and Deepak Kumar Panda. "Review—Next Generation 2D Material Molybdenum Disulfide (MoS2): Properties, Applications and Challenges". In: *ECS Journal of Solid State Science and Technology* 11.3 (Mar. 2022), p. 033012. DOI: 10.1149/2162-8777/ac5a6f. URL: https://dx.doi.org/10.1149/2162-8777/ac5a6f.

[9] A. R. Klots et al. "Probing excitonic states in suspended two-dimensional semiconductors by photocurrent spectroscopy". In: *Scientific Reports* 4.1 (Oct. 2014), p. 6608. ISSN: 2045-2322. DOI: 10.1038/srep06608. URL: https://doi.org/10.1038/srep06608.

[10] Hannu-Pekka Komsa and Arkady V. Krasheninnikov. "Effects of confinement and environment on the electronic structure and exciton binding energy of MoS_2 from first principles". In: *Phys. Rev. B* 86 (24 Dec. 2012), p. 241201. DOI: 10.1103/PhysRevB.86.241201. URL: https://link.aps.org/doi/10.1103/PhysRevB.86.241201.

[11] Ronaldo Rodrigues Pela et al. *Electronic structure of MoS_2 revisited: a comprehensive assessment of G_0W_0 calculations*. 2023. arXiv: 2310.04198 [cond-mat.mtrl-sci].

[12] Mingxiao Ye et al. "Recent Advancement on the Optical Properties of Two-Dimensional Molybdenum Disulfide (MoS2) Thin Films". In: *Photonics* 2.1 (2015), pp. 288–307. ISSN: 2304-6732. DOI: 10.3390/photonics2010288. URL: https://www.mdpi.com/2304-6732/2/1/288.

[13] Hannu-Pekka Komsa and Arkady V. Krasheninnikov. "Effects of confinement and environment on the electronic structure and exciton binding energy of MoS_2 from first principles". In: *Phys. Rev. B* 86 (24 Dec. 2012), p. 241201. DOI: 10.1103/PhysRevB.86.241201. URL: https://link.aps.org/doi/10.1103/PhysRevB.86.241201.

[14] B. Radisavljevic et al. "Single-layer MoS2 transistors". In: *Nature Nanotechnology* 6.3 (Mar. 2011), pp. 147–150. ISSN: 1748-3395. DOI: 10.1038/nnano.2010.279. URL: https://doi.org/10.1038/nnano.2010.279.

[15] Dominik Lembke and Andras Kis. "Breakdown of High-Performance Monolayer MoS2 Transistors". In: *ACS Nano* 6.11 (2012). PMID: 23039374, pp. 10070–10075. DOI: 10.1021/nn303772b. eprint: https://doi.org/10.1021/nn303772b. URL: https://doi.org/10.1021/nn303772b.

[16] Di Xiao et al. "Coupled Spin and Valley Physics in Monolayers of MoS_2 and Other Group-VI Dichalcogenides". In: *Phys. Rev. Lett.* 108 (19 May 2012), p. 196802. DOI: 10.1103/PhysRevLett.108.196802. URL: https://link.aps.org/doi/10.1103/PhysRevLett.108.196802.

[17] Shilei Ji et al. "Anomalous valley Hall effect induced by mirror symmetry breaking in transition metal dichalcogenides". In: *Phys. Rev. B* 107 (17 May 2023), p. 174434. DOI: 10.1103/PhysRevB.107.174434. URL: https://link.aps.org/doi/10.1103/PhysRevB.107.174434.

[18] Nourdine Zibouche, Martin Schlipf, and Feliciano Giustino. "GW band structure of monolayer". In: *Physical Review B* 103.12 (Mar. 2021). ISSN: 2469-9969. DOI: 10.1103/physrevb.103.125401. URL: http://dx.doi.org/10.1103/PhysRevB.103.125401.

[19] P. Khakbaz et al. "Engineering of metal-MoS2 contacts to overcome Fermi level pinning". In: *Solid-State Electronics* 194 (2022), p. 108378. ISSN: 0038-1101. DOI: https://doi.org/10.1016/j.sse.2022.108378. URL: https://www.sciencedirect.com/science/article/pii/S0038110122001502.

[20] L. H. Thomas. "The calculation of atomic fields". In: *Mathematical Proceedings of the Cambridge Philosophical Society* 23.5 (1927), pp. 542–548. DOI: 10.1017/S0305004100011683.

[21] P. Hohenberg and W. Kohn. "Inhomogeneous Electron Gas". In: *Physical Review* 136.3B (Nov. 1964), pp. 864–871. DOI: 10.1103/PhysRev.136.B864.

[22] W. Kohn and L. J. Sham. "Self-Consistent Equations Including Exchange and Correlation Effects". In: *Physical Review* 140.4A (Nov. 1965), pp. 1133–1138. DOI: 10.1103/PhysRev.140.A1133.

[23] Richard M. Martin, Lucia Reining, and David M. Ceperley. "Mean fields and auxiliary systems". In: *Interacting Electrons: Theory and Computational Approaches*. Cambridge University Press, 2016, pp. 59–83. DOI: 10.1017/CBO9781139050807.005.

[24] Richard M. Martin. "Density functional theory: foundations". In: *Electronic Structure: Basic Theory and Practical Methods*. Cambridge University Press, 2004, pp. 119–134. DOI: 10.1017/CBO9780511805769.008.

[25] Mel Levy. "Electron densities in search of Hamiltonians". In: *Phys. Rev. A* 26 (3 Sept. 1982), pp. 1200–1208. DOI: 10.1103/PhysRevA.26.1200. URL: https://link.aps.org/doi/10.1103/PhysRevA.26.1200.

[26] Elliott H. Lieb. "Density functionals for coulomb systems". In: *International Journal of Quantum Chemistry* 24.3 (1983), pp. 243–277. DOI: https://doi.org/10.1002/qua.560240302. eprint: https://onlinelibrary.wiley.com/doi/pdf/10.1002/qua.560240302. URL: https://onlinelibrary.wiley.com/doi/abs/10.1002/qua.560240302.

[27] W. Kohn. "Nobel Lecture: Electronic structure of matter—wave functions and density functionals". In: *Rev. Mod. Phys.* 71 (5 Oct. 1999), pp. 1253–1266. DOI: 10.1103/RevModPhys.71.1253. URL: https://link.aps.org/doi/10.1103/RevModPhys.71.1253.

[28] C.-O. Almbladh and U. von Barth. "Exact results for the charge and spin densities, exchange-correlation potentials, and density-functional eigenvalues". In: *Phys. Rev. B* 31 (6 Mar. 1985), pp. 3231–3244. DOI: 10.1103/PhysRevB.31.3231. URL: https://link.aps.org/doi/10.1103/PhysRevB.31.3231.

[29] D. Ceperley. "Ground state of the fermion one-component plasma: A Monte Carlo study in two and three dimensions". In: *Phys. Rev. B* 18 (7 Oct. 1978), pp. 3126–3138. DOI: 10.1103/PhysRevB.18.3126. URL: https://link.aps.org/doi/10.1103/PhysRevB.18.3126.

[30] D. M. Ceperley and B. J. Alder. "Ground State of the Electron Gas by a Stochastic Method". In: *Phys. Rev. Lett.* 45 (7 Aug. 1980), pp. 566–569. DOI: 10.1103/PhysRevLett.45.566. URL: https://link.aps.org/doi/10.1103/PhysRevLett.45.566.

[31] E. Wigner. "Effects of the electron interaction on the energy levels of electrons in metals". In: *Trans. Faraday Soc.* 34 (0 1938), pp. 678–685. DOI: 10.1039/TF9383400678. URL: http://dx.doi.org/10.1039/TF9383400678.

[32] Fabien Tran, Julia Stelzl, and Peter Blaha. "Rungs 1 to 4 of DFT Jacob's ladder: Extensive test on the lattice constant, bulk modulus, and cohesive energy of solids". In: *The Journal of Chemical Physics* 144.20 (May 2016). ISSN: 1089-7690. DOI: 10.1063/1.4948636. URL: http://dx.doi.org/10.1063/1.4948636.

[33] R. O. Jones and O. Gunnarsson. "The density functional formalism, its applications and prospects". In: *Rev. Mod. Phys.* 61 (3 July 1989), pp. 689–746. DOI: 10.1103/RevModPhys.61.689. URL: https://link.aps.org/doi/10.1103/RevModPhys.61.689.

[34] John P. Perdew, Kieron Burke, and Matthias Ernzerhof. "Generalized Gradient Approximation Made Simple". In: *Phys. Rev. Lett.* 77 (18 Oct. 1996), pp. 3865–3868. DOI: 10.1103/PhysRevLett.77.3865. URL: https://link.aps.org/doi/10.1103/PhysRevLett.77.3865.

[35] Andris Gulans et al. "exciting: a full-potential all-electron package implementing density-functional theory and many-body perturbation theory". In: *Journal of Physics: Condensed Matter* 26.36 (Aug. 2014), p. 363202. DOI: 10.1088/0953-8984/26/36/363202. URL: https://dx.doi.org/10.1088/0953-8984/26/36/363202.

[36] C Ambrosch-Draxl. "Augmented Planewave Methods". In: *Physica Scripta* 2004.T109 (Jan. 2004), p. 48. DOI: 10.1238/Physica.Topical.109a00048. URL: https://dx.doi.org/10.1238/Physica.Topical.109a00048.

[37] David J. Singh. *Planewaves, Pseudopotentials and the LAPW Method*. Springer US, 1994. ISBN: 9781475723120. DOI: 10.1007/978-1-4757-2312-0. URL: http://dx.doi.org/10.1007/978-1-4757-2312-0.

[38] D. Singh and H. Krakauer. "H-point phonon in molybdenum: Superlinearized augmented-plane-wave calculations". In: *Phys. Rev. B* 43 (2 Jan. 1991), pp. 1441–1445. DOI: 10.1103/PhysRevB.43.1441. URL: https://link.aps.org/doi/10.1103/PhysRevB.43.1441.

[39] David Singh. "Ground-state properties of lanthanum: Treatment of extended-core states". In: *Phys. Rev. B* 43 (8 Mar. 1991), pp. 6388–6392. DOI: 10.1103/PhysRevB.43.6388. URL: https://link.aps.org/doi/10.1103/PhysRevB.43.6388.

[40] I. N. YAKOVKIN and P. A. DOWBEN. "THE PROBLEM OF THE BAND GAP IN LDA CALCULATIONS". In: *Surface Review and Letters* 14.03 (June 2007), pp. 481–487. ISSN: 1793-6667. DOI: 10.1142/s0218625x07009499. URL: http://dx.doi.org/10.1142/S0218625X07009499.

[41] Xinzheng Li. *All electron G0W0 code based on FP-(L)APW+lo and applications*. 2008. DOI: 10.17169/REFUBIUM-13390. URL: https://refubium.fu-berlin.de/handle/fub188/9191.

[42] L Hedin and B I Lundqvist. "Explicit local exchange-correlation potentials". In: *Journal of Physics C: Solid State Physics* 4.14 (Oct. 1971), pp. 2064–2083. ISSN: 0022-3719. DOI: 10.1088/0022-3719/4/14/022. URL: http://dx.doi.org/10.1088/0022-3719/4/14/022.

[43] F. Aryasetiawan and O. Gunnarsson. "The GW method". In: (1997). DOI: 10.48550/ARXIV.COND-MAT/9712013. URL: https://arxiv.org/abs/cond-mat/9712013.

[44] Mark S. Hybertsen and Steven G. Louie. "First-Principles Theory of Quasiparticles: Calculation of Band Gaps in Semiconductors and Insulators". In: *Phys. Rev. Lett.* 55 (13 Sept. 1985), pp. 1418–1421. DOI: 10.1103/PhysRevLett.55.1418. URL: https://link.aps.org/doi/10.1103/PhysRevLett.55.1418.

[45] Oleg Zakharov et al. "Quasiparticle band structures of six II-VI compounds: ZnS, ZnSe, ZnTe, CdS, CdSe, and CdTe". In: *Phys. Rev. B* 50 (15 Oct. 1994), pp. 10780–10787. DOI: 10.1103/PhysRevB.50.10780. URL: https://link.aps.org/doi/10.1103/PhysRevB.50.10780.

[46] Xuejun Zhu and Steven G. Louie. "Quasiparticle band structure of thirteen semiconductors and insulators". In: *Phys. Rev. B* 43 (17 June 1991), pp. 14142–14156. DOI: 10.1103/PhysRevB.43.14142. URL: https://link.aps.org/doi/10.1103/PhysRevB.43.14142.

[47] Hong Jiang et al. "FHI-gap: A code based on the all-electron augmented plane wave method". In: *Computer Physics Communications* 184.2 (Feb. 2013), pp. 348–366. ISSN: 0010-4655. DOI: 10.1016/j.cpc.2012.09.018. URL: http://dx.doi.org/10.1016/j.cpc.2012.09.018.

[48] Takao Kotani and Mark van Schilfgaarde. "All-electron GW approximation with the mixed basis expansion based on the full-potential LMTO method". In: *Solid State Communications* 121.9–10 (Mar. 2002), pp. 461–465. ISSN: 0038-1098. DOI: 10.1016/s0038-1098(02)00028-5. URL: http://dx.doi.org/10.1016/S0038-1098(02)00028-5.

[49] Falco Hüser, Thomas Olsen, and Kristian S. Thygesen. "How dielectric screening in two-dimensional crystals affects the convergence of excited-state calculations: Monolayer MoS_2". In: *Phys. Rev. B* 88 (24 Dec. 2013), p. 245309. DOI: 10.1103/PhysRevB.88.245309. URL: https://link.aps.org/doi/10.1103/PhysRevB.88.245309.

[50] Sohrab Ismail-Beigi. "Truncation of periodic image interactions for confined systems". In: *Physical Review B* 73.23 (June 2006). DOI: 10.1103/physrevb.73.233103. URL: https://doi.org/10.1103%2Fphysrevb.73.233103.

[51] Filip A. Rasmussen and Kristian S. Thygesen. "Computational 2D Materials Database: Electronic Structure of Transition-Metal Dichalcogenides and Oxides". In: *The Journal of Physical Chemistry C* 119.23 (2015), pp. 13169–13183. DOI: 10.1021/acs.jpcc.5b02950.

[52] Filip A. Rasmussen et al. "Efficient many-body calculations for two-dimensional materials using exact limits for the screened potential: Band gaps of $\mathbf{MoS}_2$, h-BN, and phosphorene". In: *Phys. Rev. B* 94 (15 Oct. 2016), p. 155406. DOI: 10.1103/PhysRevB.94.155406. URL: https://link.aps.org/doi/10.1103/PhysRevB.94.155406.

[53] Albert Bruix et al. "Single-layer MoS_2 on Au(111): Band gap renormalization and substrate interaction". In: *Phys. Rev. B* 93 (16 Apr. 2016), p. 165422. DOI: 10.1103/PhysRevB.93.165422. URL: https://link.aps.org/doi/10.1103/PhysRevB.93.165422.

[54] Mojtaba Farmanbar and Geert Brocks. "First-principles study of van der Waals interactions and lattice mismatch at MoS_2/metal interfaces". In: *Phys. Rev. B* 93 (8 Feb. 2016), p. 085304. DOI: 10.1103/PhysRevB.93.085304. URL: https://link.aps.org/doi/10.1103/PhysRevB.93.085304.

[55] Dmitrii Nabok, Andris Gulans, and Claudia Draxl. "Accurate all-electron G_0W_0 quasiparticle energies employing the full-potential augmented plane-wave method". In: *Phys. Rev. B* 94 (3 July 2016), p. 035118. DOI: 10.1103/PhysRevB.94.035118. URL: https://link.aps.org/doi/10.1103/PhysRevB.94.035118.

[56] Kyung-Ah Min et al. "Reduction of Fermi level pinning at Au–MoS2 interfaces by atomic passivation on Au surface". In: *2D Materials* 4.1 (Nov. 2016), p. 015019. DOI: 10.1088/2053-1583/4/1/015019. URL: https://dx.doi.org/10.1088/2053-1583/4/1/015019.

[57] Antonija Grubišić Čabo et al. "Observation of Ultrafast Free Carrier Dynamics in Single Layer MoS2". In: *Nano Letters* 15.9 (Sept. 2015), pp. 5883–5887. ISSN: 1530-6984. DOI: 10.1021/acs.nanolett.5b01967. URL: https://doi.org/10.1021/acs.nanolett.5b01967.

[58] *Introduction to solid state physics*. en. 2015.

[59] Yifei Yu et al. "Engineering Substrate Interactions for High Luminescence Efficiency of Transition-Metal Dichalcogenide Monolayers". In: *Advanced Functional Materials* 26.26 (2016), pp. 4733–4739. DOI: https://doi.org/10.1002/adfm.201600418. eprint: https://onlinelibrary.wiley.com/doi/pdf/10.1002/adfm.201600418. URL: https://onlinelibrary.wiley.com/doi/abs/10.1002/adfm.201600418.

[60] Yinghui Sun, Rongming Wang, and Kai Liu. "Substrate induced changes in atomically thin 2-dimensional semiconductors: Fundamentals, engineering, and applications". In: *Appl. Phys. Rev.* 4.1 (Mar. 2017), p. 011301.

[61] Sina Lippert et al. "Influence of the substrate material on the optical properties of tungsten diselenide monolayers". In: *2D Materials* 4.2 (Mar. 2017), p. 025045. ISSN: 2053-1583. DOI: 10.1088/2053-1583/aa5b21. URL: http://dx.doi.org/10.1088/2053-1583/aa5b21.

[62] Alejandro Molina-Sánchez et al. "Temperature-dependent excitonic effects in the optical properties of single-layer¡mml:math xmlns:mml="http://www.w3.org/1998/Math/MathML"¿¡mml:msub¿¡mml
In: *Physical Review B* 93.15 (Apr. 2016). ISSN: 2469-9969. DOI: 10.1103/physrevb.93.155435. URL: http://dx.doi.org/10.1103/PhysRevB.93.155435.

[63] Soohyung Park et al. “Direct determination of monolayer MoS2and WSe2exciton binding energies on insulating and metallic substrates”. In: *2D Materials* 5.2 (Jan. 2018), p. 025003. ISSN: 2053-1583. DOI: 10.1088/2053-1583/aaa4ca. URL: http://dx.doi.org/10.1088/2053-1583/aaa4ca.